

Daniel Høyer Iversen

Improved methods for navigated 3-D vascular ultrasound imaging

Thesis for the degree of philosophiae doctor

Trondheim, 31. March 2014

Norwegian University of Science and Technology
Faculty of Medicine
Department of Circulation and Medical Imaging



NTNU – Trondheim
Norwegian University of
Science and Technology

NTNU
Norwegian University of Science and Technology

Thesis for the degree of philosophiae doctor

Faculty of Medicine
Department of Circulation and Medical Imaging

©Daniel Høyer Iversen

ISBN 978-82-326-0303-9 (electronic version)
ISBN 978-82-326-0302-2 (printed version)

Doctoral theses at NTNU,
Printed by NTNU-trykk

Improved methods for navigated 3-D vascular ultrasound imaging

Daniel Høyer Iversen

Institutt for sirkulasjon og bildediagnostikk, NTNU

Hovedveileder: Lasse Løvstakken Biveiledere: Frank Lindseth og Hans Torp

Abstract

3-D reconstruction of flow based on 2-D ultrasound images and position sensor information can be used to portray clinical information not currently available in vascular imaging. However, due to Doppler angle-dependencies and the complexity of the vascular architecture, clinical valuable 3-D information of flow direction and velocity is currently not available. The quality of the 3-D images are often not sufficient for clinical use, due to artifacts from angle dependency and too low spatial resolution. The work presented in this thesis is devoted to the development of improved quantitative and qualitative 3-D blood flow imaging based on 2-D ultrasound imaging and a position sensor system. The thesis consists of three technical contributions. The different contributions are written in article form and can be read individually. A background chapter is also included to introduce the unfamiliar reader to concepts in ultrasound imaging.

In the first paper we aim to correct for angle-dependencies in 3-D flow images based on a geometric model of the neurovascular tree generated on-the-fly from free-hand 2-D imaging and an accurate position sensor system. The 3-D vessel model acts as a priori information of vessel orientation used to angle-correct the Doppler measurements, as well as provide an estimate of the average flow direction. Based on the flow direction we were also able to do aliasing correction to approximately double the measurable velocity range.

In the second paper we aim to improve the quality of vascular 3-D images, by compounding 2-D color flow images with different steering angles. The 3-D vessel image is further generated based on navigated 3-D freehand scanning, where the position and orientation of the probe is registered by an optical sensor. This may result in higher quality 3-D flow images, without changing or complicating the clinical practice.

In the third paper we aim to generate on-the-fly 3-D images of the carotid artery from automatic segmented 2-D B-mode images based on a Kalman filter approach. During acquisition the position and orientation of each cross-sectional image of the carotid were registered by an accurate position sensor system, and further combined to reconstruct a 3-D image of the carotid artery lumen. The fast and relatively accurate reconstruction of 3-D carotid images may be suited for bedside 3-D visualization and volume estimation of moderate to large plaques.

Preface

The present thesis is submitted in partial fulfillment of the requirements for the degree of PhD at the Faculty of Medicine at the Norwegian University of Science and Technology (NTNU). The research was funded by Medical Imaging Laboratory (MI-Lab), and was carried out under the supervision of Lasse Løvstakken at the Department of Circulation and Medical Imaging, NTNU. Co-supervisors have been Frank Lindseth and Hans Torp.

Acknowledgments

Several people have been involved in the work presented in this thesis and deserve my gratitude. First of all I would like to thank my supervisor, Lasse Løvstakken. His support and guidance throughout this work has been invaluable.

I would also like to thank my colleagues and fellow PhD students in the department. Your social companionship and our technical discussions have made the days at the department fun and inspiring. I have appreciated our daily one hour lunch break.

I would also like to express my gratitude to the people at SINTEF for their help and support. A special thanks goes to my co-supervisor, Frank Lindseth. I have appreciated all the hours we have spent together in the operating room during about 25 neuro surgeries.

I have appreciated all the feedback and enthusiasm on the neuro-meetings, and I especially wish to thank neurosurgeon Geirmund Unsgård, for motivation and for never stop asking: “When can I start using this in the operating room?!”

I would also like thank friends and family for support and motivation.

Contents

1	Introduction	1
1.1	Aims of study	2
1.2	Summary of presented work	4
1.2.1	Paper 1: Model-based correction of velocity measurements in navigated 3-D ultrasound imaging during neurosurgical interventions	4
1.2.2	Paper 2: Improved quality of freehand 3-D ultrasound color flow imaging by multi-angle compounding	4
1.2.3	Paper 3: Fast 3-D reconstruction of the carotid artery bifur- cation based on real-time 2-D segmentation	5
1.3	Concluding remarks and further work	6
1.4	Thesis outline	7
1.5	List of publications	7
	References	9
2	Background	13
2.1	Ultrasound imaging	13
2.1.1	Ultrasound color flow imaging	14
2.1.2	Current limitations in color flow imaging	15
2.2	Position systems and ultrasound imaging	16
2.2.1	Center line extraction	17
2.2.2	CustusX	18
	References	19
3	Model-based correction of velocity measurements in navigated 3- D ultrasound imaging during neurosurgical interventions	23
3.1	Introduction	24
3.2	Methods	25
3.2.1	Experimental setup, acquisition and pre-processing	25
3.2.2	Model-based correction of Doppler measurements.	29
3.2.3	In vitro validation	32
3.2.4	In vivo examples	33
3.3	Results	34
3.3.1	In vitro experiments	34

3.3.2	In vivo - intracranial aneurysm and AVM	35
3.4	Discussion	36
3.5	Conclusion	43
	References	45
4	Improved quality of freehand 3-D ultrasound color flow imaging by multi-angle compounding	49
4.1	Introduction	50
4.2	Methods	51
4.2.1	Compounding of color flow data	51
4.2.2	Position sensor setup	53
4.2.3	Real-time implementation	54
4.2.4	In vitro experiments	55
4.2.5	In vivo recordings	56
4.3	Results	57
4.3.1	In vitro experiments	57
4.3.2	In vivo feasibility	58
4.4	Discussion	58
4.5	Conclusion	62
	References	63
5	Fast 3-D reconstruction of the carotid artery bifurcation based on real-time 2-D segmentation	65
5.1	Introduction	66
5.2	Methods	67
5.2.1	Experimental setup and data acquisition	67
5.2.2	On-the-fly image segmentation framework	67
5.2.3	Segmentation setup	70
5.2.4	3-D reconstruction	71
5.2.5	Data material	71
5.2.6	Validation of the segmentation algorithm	71
5.3	Results	73
5.3.1	Optimization of the segmentation parameters	73
5.3.2	Validation of the segmentation algorithm	75
5.3.3	In vivo examples	77
5.4	Discussion	80
5.5	Conclusion	83
	References	85

Chapter 1

Introduction

Ultrasound is defined as sound waves with frequencies higher than humans can hear (above 20 kHz), and has been used as a diagnostic tool for more than half a century [1]. The first commercial instruments for tissue imaging (B-mode) became available in the 1960s. First with only static images, and then with real-time B-mode images. From the late 1950s moving structures were registered with ultrasound through the Doppler shift of the received signal [2, 3]. The technique developed further and allowed for real-time two-dimensional Doppler (color flow imaging) and B-mode imaging from the mid-eighties [4]. Currently 3-D/4-D imaging and hand-held scanners are available [5, 6], and increasing computing power allows for more advanced data processing methods.

Today ultrasound imaging is used in a wide range of clinical contexts. Perhaps the most well known application is imaging of pregnant women and their unborn child. But medical ultrasound is also used extensively in cardiology, radiology, anesthesiology, gastroenterology and other disciplines of medicine. The popularity of ultrasound imaging is related to that it is non-invasive, yields real-time images, does not utilize ionizing radiation and is safe to use [7–9]. Ultrasound systems are also relatively inexpensive and portable. But medical ultrasound also has challenges and disadvantages. Ultrasound imaging works best on soft tissue, so imaging through bone is hardly possible. This makes imaging of the brain and the heart challenging due to the skull and the ribs.

Three-dimensional (3-D) ultrasound has been commercially available since 1986 [10]. Since then, the quality of 3-D scanners has improved and the range of clinical applications has grown. To generate real-time 3-D images a matrix 2-D array transducer is required, and for cardiac imaging such probes are commercial available. Currently none of these probes are optimized or available for vascular imaging. However, recent work has shown promising results for making such probes [11]. Current 3-D vascular imaging is based on generating a 3-D volume from several 2-D image slices. One such method utilizes a mechanically swept probe, basically sweeping a 1-D array in a fixed pattern. Another method requires moving the 1-D transducer array manually across the subject, with a tracking device measuring the position and the orientation. Afterwards, the 2-D images are reconstructed to

form a 3-D image. 3-D flow imaging will increase the accuracy of volume flow estimation, because both the cross-sectional area and the 3-D velocity are available. Ultrasound imaging in 3-D allows the viewer to observe the entire vascular tree, instead of searching for a single plane.

High quality flow 3-D images are especially important in the operating room where the time may be limited. During a surgery the flow conditions might change, and intraoperative flow imaging can be important to provide updated imaging data, and then offer the possibility of observing the immediate effects of surgery for quality control. The clinical benefits are further increased when integrated with navigation technology and preoperative magnetic resonance imaging data for overview and interpretation [12, 13]. In (open-skull) neurosurgery, brain shift compensation of preoperative magnetic resonance images with high spatial resolution is possible using 3-D ultrasound [14–17], which makes the combination of the two modalities an attractive solution.

The imaging of blood flow in neurosurgery is important for avoiding damage to important blood vessels during tumor surgery and for localization and quality control in neurovascular interventions. Knowing the exact location of a surgical tool relative to surrounding and infiltrating tumor vessels is crucial for a safe radical resection [18]. In other contexts, the velocity and direction of blood flow provide important information. This is especially the case for identifying the feeding vessels of intracranial arteriovenous malformations (AVMs), and is advantageous when identifying the distal branches of a complex intracranial aneurysm. Ideally, the surgeon would prefer to steer surgical instruments in the context of a high-resolution, 3-D navigation scene that properly portrays not only the vessel geometry, but also flow velocity and direction. However, because of the complex neurovascular architecture this is a challenging task, and detailed three-dimensional information of flow direction and velocity is currently not available.

Ultrasound imaging is also widely used in assessment of carotid artery stenosis. The degree of stenosis is typically based on the maximum velocity measured with ultrasound. 3-D visualization showing the geometry and extent of the plaque in the carotid artery may be clinically useful. Previous work has described a method to reconstruct 3-D B-mode images based on freehand scanning with magnetically tracking of the carotid artery for registration with MR images [19]. In [20] a custom mechanical linear 3-D ultrasound scanning system was used to generate a 3-D volume of the carotid artery. The 3-D volume was further used for manual registration of plaque volume. In [21] a 3-D volume of the carotid artery, generated from 2-D slices from a probe attached to a motorized mover, was shown to provide potentially useful information about changes in carotid plaque volume. However, none of these methods are currently available for clinical practice.

1.1 Aims of study

The overall aim of this study has been to investigate techniques which may lead to higher quality 3-D images of blood vessels. All the contributions take advantage of an optical position system, that register the position and orientation of the probe

during acquisition of 2-D ultrasound images. An increase in the image quality of reconstructed 3-D volumes may lead to a higher diagnostic certainty in neurosurgical interventions, and also for 3-D imaging of plaque in the carotid artery.

More detailed, the work aims to:

Investigate how a position system and 3-D reconstruction can be used to improve quantification and visualization of 3-D blood flow velocities.

Conventional Doppler-based ultrasound modalities are inherently limited by an angle dependency in that it is only able to measure the velocity component of blood flow in the ultrasound beam direction. When imaging complex vascular architectures such as in the neurovascular setting, the resulting images become difficult to interpret, and do not give a complete picture of the flow conditions. This is especially important in the operating room where time may be limited. With a position system the orientation of the ultrasound probe during acquisition can be registered, and from a generated 3-D geometrical vessel model the vessel orientation can be extracted. Can this additional information be used to improve the estimate of the true blood velocity and direction?

Investigate how compounding of blood flow images from different transmit angles can improve 3-D imaging of blood vessels.

Current image modalities based on the Doppler principle are insensitive to flow near perpendicular to the ultrasound beam direction. Due to the inherent complexity of the vascular architecture this causes signal drop-outs and biased blood velocity estimates in the acquired 2-D images. This further results in drop-outs or thinning of the blood vessels in the reconstructed 3-D model. It can then be difficult to interpret the resulting 3-D model, and reducing the number of drop-outs may therefore increase the diagnostic certainty when making key decisions based on image data. By imaging with different steering angles, some scan planes will be more parallel to the flow direction yielding higher Doppler shifts less influenced by the clutter filter. Can compounding of ultrasound images acquired with different steering angles thus decrease the number of drop-outs and then improve the 3-D image quality of blood vessels?

Investigate how a fast and automatic segmentation of the vessel lumen in 2-D B-mode images can be used to generate a high quality 3-D model of blood vessels.

In identification and evaluation of plaque in the carotid artery, 3-D visualization showing more accurately the geometry and extent of the plaque may be clinically useful. 3-D imaging can provide information about the distribution, volume, and degree of plaque protruding the carotid lumen. Currently, no method for 3-D ultrasound imaging of the carotid artery is clinical available. Real-time segmentation of the vessel lumen in 2-D ultrasound B-mode can be reconstructed to a 3-D model. Can combining the segmented 2-D slices to a 3-D volume provide accurate 3-D models of blood vessels?

1.2 Summary of presented work

In the following subsections, a summary of the original contributions of the thesis work will be presented.

1.2.1 Paper 1: Model-based correction of velocity measurements in navigated 3-D ultrasound imaging during neurosurgical interventions

In neurosurgery, information of blood flow is important to identify and avoid damage to important vessels. Three-dimensional intraoperative ultrasound color-Doppler imaging has proven useful in this respect. However, due to Doppler angle-dependencies and the complexity of the vascular architecture, clinical valuable 3-D information of flow direction and velocity is currently not available. In this work we aim to correct for angle-dependencies in 3-D flow images based on a geometric model of the neurovascular tree generated on-the-fly from free-hand 2-D imaging and an accurate position sensor system.

The 3-D vessel model acts as *a priori* information of vessel orientation used to angle-correct the Doppler measurements, as well as provide an estimate of the average flow direction. Based on the flow direction we were also able to do aliasing correction to approximately double the measurable velocity range. *In vitro* experiments revealed a high accuracy and robustness for estimating the mean direction of flow. Accurate angle-correction of axial velocities were possible given a sufficient beam-to-flow angle for at least parts of a vessel segment ($< 70^\circ$). *In vitro* experiments showed an absolute relative bias of 9.5% for a challenging low-flow scenario.

The method also showed promising results *in vivo*, improving the depiction of flow in the distal branches of intracranial aneurysms and the feeding arteries of an arteriovenous malformation. Careful inspection by an experienced surgeon confirmed the correct flow direction for all *in vivo* examples.

This work is described in the paper “Model-based correction of velocity measurements in navigated 3-D ultrasound imaging during neurosurgical interventions”, published in the IEEE Transactions on Medical Imaging, Vol. 39, No. 9, 2013, and presented here in its original form.

1.2.2 Paper 2: Improved quality of freehand 3-D ultrasound color flow imaging by multi-angle compounding

3-D imaging of blood flow based on 2-D ultrasound scanning and position sensor information can be used to portray clinical information not currently available in vascular and peripheral imaging. High quality 3-D color flow images are especially important in the operating room where the time may be limited. During a surgery the flow conditions might change, and intraoperative color flow imaging can be important to get updated information about blood flow and vessel structure. 3-D

intraoperative ultrasound flow imaging has proven useful in this respect. However, due to Doppler angle-dependencies and the complexity of the vascular architecture, the generated 3-D image of blood vessels often have drop-outs in the vessel structure.

In this work we aim to reduce the number of drop-outs in the 3-D blood flow images by combining 2-D flow images with different steering angles. The compounded 2-D images are further reconstructed to a 3-D flow image based on information from an accurate position sensor system. The method was implemented on a research ultrasound scanner for real-time processing of the data, and in vitro trials showed promising results. The method also showed promising results in vivo using a clinical approved high-end scanner, improving the 3-D image quality of the feeding arteries of an arteriovenous malformation.

This work is described in the paper “Improved quality of freehand 3-D ultrasound color flow imaging by multi-angle compounding”

1.2.3 Paper 3: Fast 3-D reconstruction of the carotid artery bifurcation based on real-time 2-D segmentation

Stroke is currently the second leading cause of death worldwide, with a prevalence that is expected to increase in the coming years due to the aging population and lifestyles associated with obesity. Plaque in the carotid artery is responsible for approximately 20% of all strokes of thromboembolic origin. Hence, improved diagnostic methods to detect and understand the progression of diseases in the carotid artery is considered important. Due to the three-dimensional (3-D) extent of the plaque, 3-D imaging is desired in order to provide information about the distribution, volume, and degree of plaque protruding the carotid lumen. However, due to current non-availability of 3-D vascular ultrasound probes this is currently not possible.

In this work we aim to reconstruct on-the-fly 3-D models of the carotid artery from automatically segmented 2-D ultrasound images using a Kalman filter approach. During acquisition the position and orientation of each cross-sectional image of the carotid were registered by an accurate position sensor system, and further combined to reconstruct a 3-D model of the carotid artery lumen. The parameters in the automatic segmentation algorithm were tuned on a test set consisting of data from five people. A manual segmentation done by two experts evaluators, resulting in an inter-observer error similar to the error of the manual segmentation compared with the automatic segmentation. The fast and relatively accurate reconstruction of 3-D carotid models may be suited to bedside 3-D visualization and volume estimation of moderate to large plaques.

This work is described in the paper “Fast 3-D reconstruction of the carotid artery bifurcation based on real-time 2-D segmentation”

1.3 Concluding remarks and further work

Due to angle-dependencies it is normally not possible to estimate the true velocity of the blood in ultrasound color flow imaging. In paper 1 the velocities are angle-corrected using a model-based approach and information from the position system. Hence, an improved estimate of the true velocity can be given automatically. Based on the velocities and information from the position system a robust estimate of the true flow direction can also be estimated. The next step would be to test the method in the operating room during neuro surgery for a larger patient material in order to map the methods' clinical utility. The method requires a continuous centerline representation of the blood vessels, and that required a manual step when the paper was written. A new algorithm to find the center line is now available [22], but the robustness of the method for neuro angio data still remains to be tested. Video grabbing has been used to acquire data for generating 3-D models, but velocity data are required for angle correction. Now all required data can be streamed over a network protocol from the scanner. This gives access to all necessary data, and might also lead to higher quality of the 3-D model.

Imaging at near perpendicular beam-to-flow angles will result in drop-outs in the 3-D images. In paper 2 compounding of color flow images from different steering angles are used to reduce the number of drop-outs. The technique can reduce the number of drop-outs in the 3-D volume of blood vessels, and may particularly improve the 3-D image of neurovascular flow, where imaging of small vessels in a potentially complicated vascular network. Further work should implement the transmit sequence on a high-end ultrasound system for real-time imaging. This allows for testing for a larger patient population. If a larger patient study shows promising results, the method can easily be adopted in a clinical practice.

In paper 1 a higher uncertainty in angle-correction of near perpendicular beam-to-flow angles was observed. By using compounding of different angles to estimate the color flow image image, a higher certainty of estimated velocities can be achieved. This approach remains to be tried. Less dropouts in the 3-D model will also simplify extraction of the centerline required for angle-correcting the velocity. An accurate centerline can also improve brain shift correction of pre-operative MR images.

It is challenging to obtain high quality 3-D volumes of the carotid artery from 2-D ultrasound color flow images due to pulsatile flow and a wide span of blood velocities. Therefore, in paper 3 a real-time segmentation of the tissue images are used to generate 3-D images of the carotid artery. The method should be further tested on a larger patient population to map the potential clinical utility. The method could also be tested on other blood vessels than the carotid artery. It would for instance be interesting to see how the method works on blood vessels in the brain. It might be possible to do the segmentation in 3-D where a preoperative MR image is available as an initial model for regularization.

The methods presented here will to some extent improve the 3-D image quality of blood vessels. Hopefully, this thesis work may be continued to investigate further the future work aspects described and to further refine the image quality in 3D ultrasound.

1.4 Thesis outline

The thesis is organized as follows: In chapter 2, a short background for the techniques applied in this work is included for the unfamiliar reader to understand the problems and work presented in the following chapters. Finally, in chapter 3-5 the papers are presented. The papers are included as originally published, but have been adapted to the book layout.

1.5 List of publications

Papers included in the thesis

1. **Daniel Høyer Iversen**, Frank Lindseth, Geirmund Unsgaard, Hans Torp and Lasse Lovstakken, “*Model-based correction of velocity measurements in navigated 3-D ultrasound imaging during neurosurgical interventions*”, IEEE Transactions on Medical Imaging, Vol. 39, No. 9, 2013
2. **Daniel Høyer Iversen**, Frank Lindseth, Geirmund Unsgaard, Hans Torp and Lasse Lovstakken, “*Improved quality of freehand 3-D ultrasound color flow imaging by multi-angle compounding*”
3. **Daniel Høyer Iversen**, Sigurd Storve, Torbjørn Dahl, Hans Torp and Lasse Lovstakken, “*Fast 3-D reconstruction of the carotid artery bifurcation based on real-time 2-D segmentation*”

Relevant papers and conference proceedings that are not included in the thesis

1. **Daniel Høyer Iversen**, Frank Lindseth, Geirmund Unsgaard, Hans Torp and Lasse Lovstakken, “*Model-based correction of angle-dependencies in navigated 3-D flow imaging during neurosurgical interventions*”, IEEE International ultrasonics Symposium Proceedings 2011
2. **Daniel Høyer Iversen**, Frank Lindseth, Hans Torp and Lasse Lovstakken, “*Improved 3-D reconstruction of vascular flow based on plane wave imaging*”, IEEE International Ultrasonics Symposium Proceedings 2012
3. Ingerid Reinertsen, Frank Lindseth, Christian Askeland, **Daniel Høyer Iversen** and Geirmund Unsgaard, “*Intraoperative correction of brain-shift*”, accepted for publication in Acta Neurochirurgica.

REFERENCES

- [1] B. Angelsen, “Ultrasound imaging: Waves, signals, and signal processing,” *Emantec*, 2000.
- [2] I. Edler and C. Hertz, “The use of ultrasonic reflectoscope for the continuous recording of the movements of heart walls.” *Kunagl fysiogr sallsk*, vol. 24, no. 5, 1954. [Online]. Available: <http://onlinelibrary.wiley.com/doi/10.1111/j.1475-097X.2004.00539.x/full>
- [3] S. Satomura, “Ultrasonic Doppler method for the inspection of cardiac functions,” *J. Acoust. Soc. Am*, vol. 29, p. 1181, 1957.
- [4] K. Beach, “1975-2000: a quarter century of ultrasound technology,” *Ultrasound in medicine & biology*, vol. 18, no. 4, pp. 377–388, 1992. [Online]. Available: <http://www.sciencedirect.com/science/article/pii/S030156299290046D>
- [5] C. Ligtoet, H. Rusterborgh, L. Kappen, and N. Bom, “Real time ultrasonic imaging with a hand-held scanner Part I: Technical description,” *Ultrasound in medicine & biology*, vol. 4, no. 2, pp. 91–92, 1978.
- [6] J. B. Seward, P. S. Douglas, R. Erbel, R. E. Kerber, I. Kronzon, H. Rakowski, L. D. J. Sahn, E. J. Sisk, A. J. Tajik, and S. Wann, “Hand-carried cardiac ultrasound (HCU) device: recommendations regarding new technology. A report from the Echocardiography Task Force on New Technology of the Nomenclature and Standards Committee of the American Society of Echocardiography,” *Journal of the American Society of Echocardiography*, vol. 15, no. 4, pp. 369–373, 2002.
- [7] S. B. Barnett, G. R. Ter Haar, M. C. Ziskin, W. L. Nyborg, K. Maeda, and J. Bang, “Current status of research on biophysical effects of ultrasound,” *Ultrasound in medicine & biology*, vol. 20, no. 3, pp. 205–218, 1994.
- [8] S. B. Barnett, G. R. Ter Haar, M. C. Ziskin, H.-D. Rott, F. A. Duck, and K. Maeda, “International recommendations and guidelines for the safe use of diagnostic ultrasound in medicine,” *Ultrasound in medicine & biology*, vol. 26, no. 3, pp. 355–366, 2000.

-
- [9] S. B. Barnett and D. Maulik, “Guidelines and recommendations for safe use of Doppler ultrasound in perinatal applications,” *Journal of Maternal-Fetal and Neonatal Medicine*, vol. 10, no. 2, pp. 75–84, 2001.
- [10] R. W. Prager, U. Z. Ijaz, a. H. Gee, G. M. Treece, and P. N. T. Wells, “Three-dimensional ultrasound imaging,” *Proceedings of the Institution of Mechanical Engineers, Part H: Journal of Engineering in Medicine*, vol. 224, no. 2, pp. 193–223, Feb. 2010. [Online]. Available: <http://pih.sagepub.com/lookup/doi/10.1243/09544119JEIM586>
- [11] M. W. Docter, R. Beurskens, G. Ferin, P. J. Brands, J. G. Bosch, and N. de Jong, “A matrix phased array system for 3D high frame-rate imaging of the carotid arteries,” in *Ultrasonics Symposium (IUS), 2010 IEEE*. IEEE, 2010, pp. 318–321.
- [12] A. Gronningsaeter, A. Kleven, S. Ommedal, T. E. Aarseth, T. Lie, F. Lindseth, T. Langø, and G. Unsgaard, “SonoWand, an Ultrasound-based Neuronavigation System,” *Neurosurgery*, vol. 47, no. 6, pp. 1373–1380, Dec. 2000. [Online]. Available: <http://content.wkhealth.com/linkback/openurl?sid=WKPTLP:landingpage&an=00006123-200012000-00021>
- [13] W. Tirakotai, D. Miller, S. Heinze, L. Benes, H. Bertalanffy, and U. Sure, “A novel platform for image-guided ultrasound,” *Neurosurgery*, vol. 58, no. 4, p. 710, 2006.
- [14] V. A. Coenen, T. Krings, J. Weidemann, F. J. Hans, P. Reinacher, J. M. Gilsbach, and V. Rohde, “Sequential visualization of brain and fiber tract deformation during intracranial surgery with three-dimensional ultrasound: an approach to evaluate the effect of brain shift,” *Neurosurgery*, vol. 56, no. 1, p. 133, 2005.
- [15] I. A. Rasmussen, F. Lindseth, O. M. Rygh, E. M. Berntsen, T. Selbekk, J. Xu, T. A. Nagelhus Hernes, E. Harg, A. Håberg, and G. Unsgaard, “Functional neuronavigation combined with intra-operative 3D ultrasound: initial experiences during surgical resections close to eloquent brain areas and future directions in automatic brain shift compensation of preoperative data,” *Acta neurochirurgica*, vol. 149, no. 4, pp. 365–378, 2007.
- [16] I. Reinertsen, F. Lindseth, G. Unsgaard, and D. L. Collins, “Clinical validation of vessel-based registration for correction of brain-shift,” *Medical image analysis*, vol. 11, no. 6, pp. 673–684, Dec. 2007. [Online]. Available: <http://linkinghub.elsevier.com/retrieve/pii/S1361841507000679>
- [17] U. Sure, L. Benes, O. Bozinov, M. Woydt, W. Tirakotai, and H. Bertalanffy, “Intraoperative landmarking of vascular anatomy by integration of duplex and Doppler ultrasonography in image-guided surgery. Technical note,” *Surgical neurology*, vol. 63, no. 2, pp. 133–142, 2005.

REFERENCES

- [18] O. M. Rygh, T. A. Nagelhus Hernes, F. Lindseth, T. Selbekk, T. Brostrup Müller, and G. Unsgaard, “Intraoperative navigated 3-dimensional ultrasound angiography in tumor surgery,” *Surgical Neurology*, vol. 66, no. 6, pp. 581–592, Dec. 2006. [Online]. Available: <http://linkinghub.elsevier.com/retrieve/pii/S0090301906006355>
- [19] P. Slomka, J. Mandel, D. Downey, and A. Fenster, “Evaluation of voxel-based registration of 3-D power Doppler ultrasound and 3-D magnetic resonance angiographic images of carotid arteries,” *Ultrasound in medicine & ...*, vol. 27, no. 7, pp. 945–955, 2001. [Online]. Available: <http://www.sciencedirect.com/science/article/pii/S0301562901003878>
- [20] A. Landry, C. Ainsworth, C. Blake, and J. D. Spence, “Manual planimetric measurement of carotid plaque volume using three-dimensional ultrasound imaging,” *Medical physics*, vol. 34, pp. 1496–1505, 2007.
- [21] C. D. Ainsworth, C. C. Blake, A. Tamayo, V. Beletsky, A. Fenster, and J. D. Spence, “3D ultrasound measurement of change in carotid plaque volume: a tool for rapid evaluation of new therapies.” *Stroke; a journal of cerebral circulation*, vol. 36, no. 9, pp. 1904–9, Sep. 2005. [Online]. Available: <http://www.ncbi.nlm.nih.gov/pubmed/16081857>
- [22] E. Smistad, A. C. Elster, and F. Lindseth, “GPU accelerated segmentation and centerline extraction of tubular structures from medical images.” *International journal of computer assisted radiology and surgery*, no. 7491, Nov. 2013. [Online]. Available: <http://www.ncbi.nlm.nih.gov/pubmed/24177985>

Chapter 2

Background

The following sections contains a brief introduction to diagnostic ultrasound in general. It also includes more details about blood flow imaging and navigated ultrasound imaging. The purpose is to provide the unfamiliar reader with some background, that might be helpful in understanding the papers included in the thesis. For a more extensive description of the topics, please refer to [1, 2] for general medical ultrasound topics, [3] for more knowledge about blood flow imaging and [4] for more information about position systems and ultrasound based guidance.

2.1 Ultrasound imaging

The generation of ultrasound images are based on transmission of a sound pulse. In diagnostic ultrasound the ultrasound frequency is between 2-40 MHz. Boundaries between different soft tissues and heterogeneities within the tissue with different acoustic properties, causes reflection and scattering of the ultrasound. By assuming a constant speed of sound, c , the depth, z , to different objects in the body can be calculated as

$$z = \frac{ct}{2}. \quad (2.1)$$

Where, t , is the time it takes for the echo to return to the ultrasound probe. The pressure amplitude of the backscattered signal is registered and used to generate an image.

The transmitted ultrasound field is attenuated during its progression through tissue, and the attenuation increases with increasing frequency. For soft tissue a value of 0.5 dB/cm MHz is often used [5]. The attenuation in the brain seems to be higher, and in [6] the attenuation of brain tissue acquired in 20 brain operations is reported to be 0.94 ± 0.13 dB/cm MHz. The large attenuation for brain suggest that the ultrasound pulse will be more damped in brain tissue than in most other soft tissue.

The spatial resolution of an ultrasound image is proportional to the frequency of the transmitted pulse, so one would in principle use higher frequencies. Since the

attenuation also depends of the frequency, a compromise between penetration depth and resolution must be accepted. So for imaging of brain tissue a lower frequency is required to get sufficient backscattered signal. Hence a lower resolution is obtained, and structures will appear to be more smeared out.

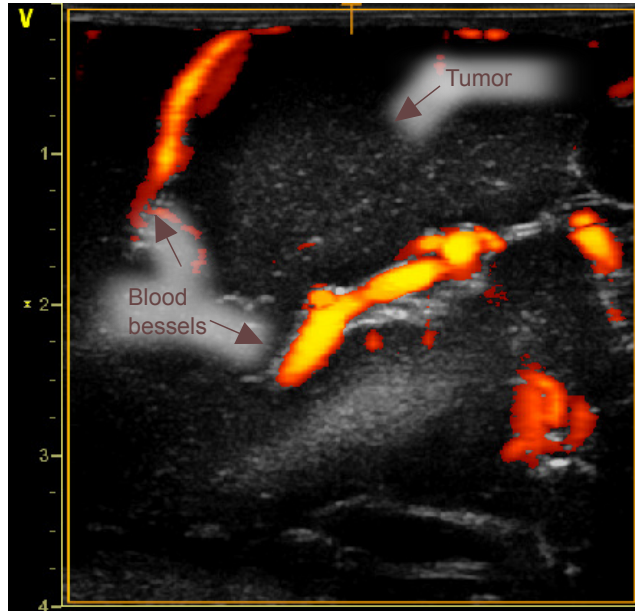


Figure 2.1: Ultrasound image of a tumor with blood vessels very close by.

2.1.1 Ultrasound color flow imaging

All modern ultrasound scanners have a mode for 2-D imaging of blood vessels, often called color flow imaging (CFI). In Fig. 2.1 an example with tissue image and an overlaying flow image is shown. A transmitted ultrasound pulse from a moving scatterer is reflected with a shift in frequency due to the Doppler effect. In practice it is hard to measure the change in frequency originating from the Doppler effect due to frequency dependent attenuation. Instead a series of ultrasound pulses are transmitted at a certain pulse repetition frequency (PRF), and the rate of change in the phase returning from a certain sample volume is normally used to estimate the color flow images.

Unfortunately the backscattered signal from blood is much weaker than from tissue. But the velocity of blood scatters is normally higher than the velocity of the tissue, so a high pass filter can be used to separate the blood signal. However, the filter will also remove components of low velocity flow and limiting the minimum measurable velocity. Several clutter filters have been studied in the past, including FIR filters, IIR filters and polynomial filters [7–9]. In this work polynomial regression filters are used. A polynomial regression filter have a smooth and monotonic

frequency response. For equal stopband width, the polynomial regression filter has a shorter transition region than FIR filters. An additional reduction in variance of the autocorrelation estimates may also be achieved as no samples need to be discarded after filtering [10]. But regression filters are not time invariant, which causes frequency distortion in the transition band of the filter [8]. For a polynomial regression filter is the -3dB cut-off velocity in the probe direction given in [11] as

$$v_{-3\text{dB}} \approx 0.42 \cdot \frac{N+1}{M} \cdot 2v_{\text{Nyq}}. \quad (2.2)$$

Here N is the filter order of the polynomial regression filter and M is the number of pulse emissions (ensemble size). The minimum detectable blood flow velocity in the flow direction will then be

$$v_{\text{min}} = \frac{v_{-3\text{dB}}}{\cos(\theta)}, \quad (2.3)$$

where θ is the angle between the flow direction and the beam direction. The minimum detectable blood flow velocity in the flow direction increases as the angle θ increases. So for an angle $\theta = 60^\circ$ the minimum detectable flow is $2v_{-3\text{dB}}$ in the flow direction.

To estimate the blood velocity demodulated in-phase and quadrature data (IQ-data) are high-pass filtered to isolate the signal from moving blood. Then the autocorrelation data with lag, l , is estimated as described in [12] from the filtered IQ-data:

$$R(l) = \frac{1}{M-l} \sum_{k=1}^{M-l} z(k+l)z(k)^*, \quad (2.4)$$

where z is the IQ-data ensemble from one point in the 2-D frame and z^* is the complex conjugate of z . The sum is over the ensemble of pulse emissions (ensemble size), M . The power of the backscattered signal is estimated from $R(0)$, while the velocity along the ultrasound beam axis is estimated as

$$v = \frac{\angle R(1)}{\pi} \cdot v_{\text{Nyq}}. \quad (2.5)$$

Where \angle is the complex phase angle and

$$v_{\text{Nyq}} = \frac{c \cdot \text{PRF}}{4f_0}. \quad (2.6)$$

Here c is the speed of sound in blood (1560m/s), PRF is the Doppler pulse repetition frequency and f_0 is the received pulse center frequency. Both estimated velocity and power can be used for visualization of the blood vessels.

2.1.2 Current limitations in color flow imaging

Traditional color flow imaging is limited to estimate the velocity along the ultrasound beam axis. So only a one-dimensional component of the velocity can be

measured, but the true blood flow is three-dimensional. This is a major limitation in blood flow imaging, and both the power and velocity images will depend of the probe orientation according to the blood vessels. Due to the angle dependency, interpretation of 2-D flow images can be difficult, and for 3-D images interpretation of the blood flow is even harder.

In color flow imaging the range of measurable velocities is frequently insufficient for capturing both the low and high flow velocities. The maximum measurable velocity, given from the Nyquist sampling theorem, is called the Nyquist velocity, v_{Nyq} . The lower limit regarding detection and estimation of blood velocities in the beam direction is in practice determined by the clutter filter properties. So a low axial velocity in the beam direction will lead to a signal drop-out in the acquired 2-D image. Resulting in drop-outs or thinning of the blood vessels in the 3-D image. For a complex vascular architecture it can then be difficult to interpret the resulting 3-D model of the blood vessels.

Less signal is backscattered from blood than for normal tissue, so a lower frequency is normally used for flow imaging than for B-mode imaging. This also lead to a lower spatial resolution for blood flow imaging and a smearing of the structures. Due to an inadequate spatial resolution can it in some cases seems incorrectly that blood vessels are connected.

3-D Flow imaging has some challenging due to imaging of moving objects and the pulsatile flow. The 2-D images are acquired at different states in the heart cycle, leading to variation along the blood vessel. Both the diameter and the velocity are changing during the heart cycle influencing the finale 3-D image.

Flashing artifacts in the image can occur during freehand scan due to abrupt movement of the ultrasound probe, or due to tissue movement caused by pulsatile flow. A flash will appear as a big bubble in the 3-D scene, and complicate the interpretation of the vessel structure.

2.2 Position systems and ultrasound imaging

By tracking the orientation and position of the ultrasound probe, 3-D images can be generated from acquired 2-D ultrasound images. Further, the position of tracked surgical tools can be visualized in the generated 3-D scene. An example of such a setup is shown in Fig. 2.2. Here the ultrasound scanner, the tracking system and the navigation system can be seen.

To track the position and orientation of an ultrasound probe a position system is required. Different tracking technologies are used for measuring the positions and orientations: mechanical, acoustical (where ultrasound actually is used for tracking), electromagnetic and optical [13]. In the work presented in this thesis we have used an optical tracking system with two cameras to track passive (infrared light reflectors) markers placed in a rigidly defined geometry on the ultrasound probe. We have used a system from NDI Polaris Spectra (Northern Digital, Waterloo, Canada), as seen in Fig. 2.2. The position of the markers differs from that of the ultrasound image, but since this sensor is fixed to the probe, the spatial relationship between the sensor and the image is constant. A probe calibration has to be

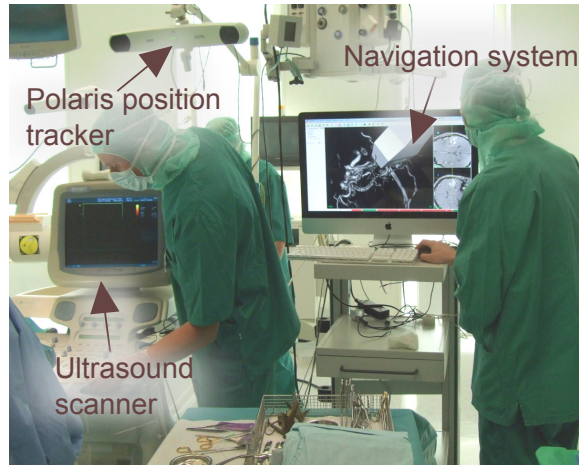


Figure 2.2: A navigation system and an ultrasound scanner during a brain surgery. Here the ultrasound scanner, the tracking system and the navigation system can be seen.

done to find this relationship, and several different calibration methods exist [14]. We have used a method where a sphere, with a position known from the position system, is identified in ultrasound images several times for different positions of the sphere. Since the signal from the position system and the ultrasound data have separate time delays, a temporal calibration is necessary [15, 16]. Small errors in the spatial or temporal calibration will lead to inaccuracies in the 3-D model.

When using tracked 2-D probes a freehand scan is performed and the 3-D image is created with a 3-D reconstruction algorithm. There exist different algorithms for reconstructing 3-D volumes from freehand 2-D ultrasound images, but we have used a Pixel Nearest Neighbor algorithm as described in [17]. Each pixel in the 2-D images is added to the nearest voxel in a 3-D volume. Afterwards an interpolation step is usually performed to fill empty voxels.

An alternative to a position system is to use a 3-D probe that can provide 3-D volumes directly. A 3-D probe will allow more easy acquisition and real-time 3-D data. The main advantages of using a tracked 2-D probe are that larger volume can be covered and the resolution is much higher than for currently available 3-D probes. A 3-D linear array suited for vascular imaging requires a higher frequency and a high amount of elements to cover a sufficient field of view. However, previous work has shown the possibility of such probes [18–21], so commercial probes suited for vascular flow imaging might soon be available.

2.2.1 Center line extraction

From the 3-D image of the blood vessels a center line can be extracted. The center line can provide geometrical information about the blood vessels, and can be used for shift correction of preoperative MR data. We have used a method based on a

3-D thinning algorithm, where the blood vessels iteratively are thinned until only the center points are left [22]. Another method are presented in [23] that provides a connected center line based on a fast GPU-algorithm. A connected center line provides extra information about the vessel geometry.

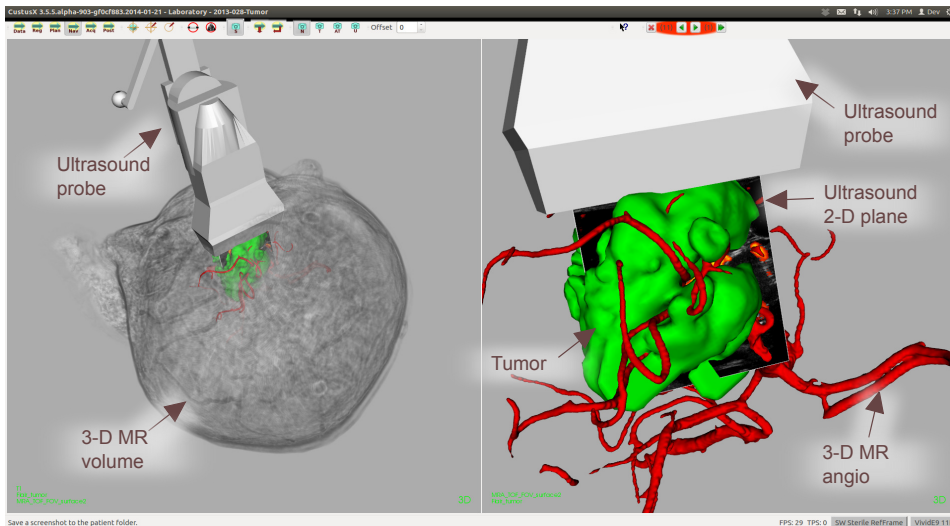


Figure 2.3: Screenshot from CustusX during acquisition of ultrasound data of a brain tumor.

2.2.2 CustusX

We have used an in-house navigation system called CustusX [24], developed by SINTEF Medical technology (Health Research, Trondheim, Norway). CustusX is an application for research in image-guided therapy with a focus on intraoperative use and ultrasound imaging, see Fig. 2.2 and Fig. 2.3. The system can handle preoperative images from magnetic resonance (MR). The MR images are registered to the patient before the surgery, and intraoperative ultrasound is used for moving the MR images to the correct position by matching the center line of the blood vessels [25, 26]. During surgery CustusX can be used to provide updated 3-D ultrasound images of both tissue and blood vessels.

REFERENCES

- [1] T. L. Szabo, *Diagnostic ultrasound imaging: inside out*. Academic Press, 2004.
- [2] R. S. C. Cobbold, “Foundations of Biomedical Ultrasound,” *Distribution*, 2002.
- [3] J. r. A. Jensen, *Estimation of blood velocities using ultrasound: a signal processing approach*. Cambridge University Press, 1996.
- [4] F. Lindseth, T. Langø, T. Selbekk, R. Hansen, I. Reinertsen, C. Askeland, O. Solheim, G. Unsgård, R. Mårvik, and T. A. N. Hernes, “Ultrasound-Based Guidance and Therapy, Advancements and Breakthroughs in Ultrasound Imaging,” 2013. [Online]. Available: <http://www.intechopen.com/books/export/citation/BibTex/advancements-and-breakthroughs-in-ultrasound-imaging/ultrasound-based-guidance-and-therapy>
- [5] B. Angelsen, “Ultrasound imaging: Waves, signals, and signal processing,” *Emantec*, 2000.
- [6] M. Strowitzki, S. Brand, and K.-V. Jenderka, “Ultrasonic radio-frequency spectrum analysis of normal brain tissue.” *Ultrasound in medicine & biology*, vol. 33, no. 4, pp. 522–9, Apr. 2007. [Online]. Available: <http://www.ncbi.nlm.nih.gov/pubmed/17316962>
- [7] A. Hoeks and J. V. de Vorst, “An efficient algorithm to remove low frequency Doppler signals in digital Doppler systems,” *Ultrasonic imaging*, vol. 144, pp. 135–144, 1991. [Online]. Available: <http://www.sciencedirect.com/science/article/pii/0161734691900802>
- [8] H. Torp, “Clutter rejection filters in color flow imaging: a theoretical approach.” *IEEE transactions on ultrasonics, ferroelectrics, and frequency control*, vol. 44, no. 2, pp. 417–24, Jan. 1997. [Online]. Available: <http://www.ncbi.nlm.nih.gov/pubmed/18244139>
- [9] S. Bjærum, H. Torp, and K. Kristoffersen, “Clutter Filter Design for Ultrasound Color Flow Imaging,” *Ultrasonics, Ferroelectrics and Frequency Control, IEEE Transactions on*, vol. 49, no. 2, pp. 204–216, 2002.

-
- [10] S. Bjærum, “Detection and Visualization of Moving Targets in Medical Ultrasound Imaging,” *PhD thesis, NTNU*, 20001.
- [11] S. Bjærum, H. Torp, T. r. Bakke, and K. Kristoffersen, “Automatic Selection of the Clutter Filter Cut-off Frequency in Ultrasound Color Flow Imaging,” *Ultrasonics, Ferroelectrics and Frequency Control, IEEE Transactions on*, vol. 49, no. 2, pp. 204–216, 2002.
- [12] C. Kasai, K. Namekawa, A. Koyano, and R. Omoto, “Real-time two-dimensional blood flow imaging using an autocorrelation technique,” *IEEE Trans. Sonics Ultrason*, vol. 32, no. 3, pp. 458–464, 1985. [Online]. Available: http://server.elektro.dtu.dk/personal/jaj/31545/documents/kasai_et_al.1985.pdf
- [13] P. Cinquin, E. Bainville, and C. Barbe, “Computer assisted medical interventions,” *Engineering in Medicine and Biology Magazine, IEEE*, vol. 14, no. 3, pp. 254–263, 1995. [Online]. Available: http://ieeexplore.ieee.org/xpls/abs_all.jsp?arnumber=391779
- [14] L. Mercier, T. Langø, F. Lindseth, and D. L. Collins, “A review of calibration techniques for freehand 3-D ultrasound systems,” *Ultrasound in medicine & biology*, vol. 31, no. 4, pp. 449–471, 2005.
- [15] G. M. Treece, A. H. Gee, R. W. Prager, C. J. Cash, and L. H. Berman, “High-definition freehand 3-D ultrasound,” *Ultrasound in Medicine & Biology*, vol. 29, no. 4, pp. 529–546, Apr. 2003. [Online]. Available: <http://linkinghub.elsevier.com/retrieve/pii/S0301562902007354>
- [16] F. Rousseau, P. Hellier, and C. Barillot, “A novel temporal calibration method for 3-D ultrasound.” *IEEE transactions on medical imaging*, vol. 25, no. 8, pp. 1108–12, Aug. 2006. [Online]. Available: <http://www.ncbi.nlm.nih.gov/pubmed/16895003>
- [17] O. V. Solberg, F. Lindseth, H. Torp, R. E. Blake, and T. Nagelhus Hernes, “Freehand 3D ultrasound reconstruction algorithms—a review.” *Ultrasound in medicine & biology*, vol. 33, no. 7, pp. 991–1009, Jul. 2007. [Online]. Available: <http://www.ncbi.nlm.nih.gov/pubmed/17512655>
- [18] R. W. Prager, U. Z. Ijaz, a. H. Gee, G. M. Treece, and P. N. T. Wells, “Three-dimensional ultrasound imaging,” *Proceedings of the Institution of Mechanical Engineers, Part H: Journal of Engineering in Medicine*, vol. 224, no. 2, pp. 193–223, Feb. 2010. [Online]. Available: <http://pih.sagepub.com/lookup/doi/10.1243/09544119JEIM586>
- [19] M. J. Pihl and J. A. Jensen, “3D vector velocity estimation using a 2D phased array,” *2011 IEEE International Ultrasonics Symposium*, pp. 430–433, Oct. 2011. [Online]. Available: <http://ieeexplore.ieee.org/lpdocs/epic03/wrapper.htm?arnumber=6293083>

REFERENCES

- [20] M. J. Pihl and J. A. Jensen, "Measuring 3D velocity vectors using the Transverse Oscillation method," *2012 IEEE International Ultrasonics Symposium*, pp. 1881–1885, Oct. 2012. [Online]. Available: <http://ieeexplore.ieee.org/lpdocs/epic03/wrapper.htm?arnumber=6561897>
- [21] M. W. Docter, R. Beurskens, G. Ferin, P. J. Brands, J. G. Bosch, and N. de Jong, "A matrix phased array system for 3D high frame-rate imaging of the carotid arteries," in *Ultrasonics Symposium (IUS), 2010 IEEE*. IEEE, 2010, pp. 318–321.
- [22] T. Lee and R. Kashyap, "Building skeleton models via 3-D medial surface/axis thinning algorithms," *CVGIP: Graphical Model and Image*, 1994.
- [23] E. Smistad, A. C. Elster, and F. Lindseth, "GPU accelerated segmentation and centerline extraction of tubular structures from medical images." *International journal of computer assisted radiology and surgery*, no. 7491, Nov. 2013. [Online]. Available: <http://www.ncbi.nlm.nih.gov/pubmed/24177985>
- [24] C. Askeland, F. Lindseth, O. V. Solberg, J. Beate, L. Bakeng, and G. A. Tangen, "CustusX : A Research Application for Image-Guided Therapy," *Insight Journal*, pp. 1–8, 2011.
- [25] O. M. Rygh, T. A. Nagelhus Hernes, F. Lindseth, T. Selbekk, T. Brostrup Muller, and G. Unsgaard, "Intraoperative navigated 3-dimensional ultrasound angiography in tumor surgery," *Surgical neurology*, vol. 66, no. 6, pp. 581–592, 2006.
- [26] I. Reinertsen, F. Lindseth, G. Unsgaard, and D. L. Collins, "Clinical validation of vessel-based registration for correction of brain-shift," *Medical image analysis*, vol. 11, no. 6, pp. 673–684, Dec. 2007. [Online]. Available: <http://linkinghub.elsevier.com/retrieve/pii/S1361841507000679>

Chapter 3

Model-based correction of velocity measurements in navigated 3-D ultrasound imaging during neurosurgical interventions

Daniel Høyer Iversen¹, Frank Lindseth^{2,3}, Geirmund Unsgaard⁴, Hans Torp¹ and Lasse Lovstakken^{1,5}

¹MI Lab and Dept. of Circulation and Medical Imaging, Norwegian University of Science and Technology, Trondheim, Norway

² SINTEF Medical Technology, Trondheim, Norway

³Department of Computer and Information Science, Norwegian University of Science and Technology, Trondheim, Norway

⁴ Department of Neurosurgery, Trondheim University Hospital, Norway

⁵ Trondheim University Hospital, Norway

Abstract — In neurosurgery, information of blood flow is important to identify and avoid damage to important vessels. Three-dimensional intraoperative ultrasound color-Doppler imaging has proven useful in this respect. However, due to Doppler angle-dependencies and the complexity of the vascular architecture, clinical valuable 3-D information of flow direction and velocity is currently not available. In this work we aim to correct for angle-dependencies in 3-D flow images based on a geometric model of the neurovascular tree generated on-the-fly from free-hand 2-D imaging and an accurate position

sensor system. The 3-D vessel model acts as a priori information of vessel orientation used to angle-correct the Doppler measurements, as well as provide an estimate of the average flow direction. Based on the flow direction we were also able to do aliasing correction to approximately double the measurable velocity range. *In vitro* experiments revealed a high accuracy and robustness for estimating the mean direction of flow. Accurate angle-correction of axial velocities were possible given a sufficient beam-to-flow angle for at least parts of a vessel segment ($< 70^\circ$). *In vitro* experiments showed an absolute relative bias of 9.5% for a challenging low-flow scenario. The method also showed promising results *in vivo*, improving the depiction of flow in the distal branches of intracranial aneurysms and the feeding arteries of an arteriovenous malformation. Careful inspection by an experienced surgeon confirmed the correct flow direction for all *in vivo* examples.

3.1 Introduction

In neurosurgery, information about blood flow can be important to avoid damage to vessels during tumor resection, to identify the feeding arteries of arteriovenous malformations (AVMs), and is advantageous when identifying and securing flow in the distal branches of intracranial aneurysms after clipping. Currently MR angiography is the leading image modality for mapping blood flow in the brain preoperatively [1]. Intraoperative 3-D ultrasound imaging is a cost and time efficient modality that has proven useful for providing updated information about the vessel structures and blood flow during the operation, as brain deformation after skull opening renders preoperative MR images inaccurate [2, 3].

Current methods for real-time ultrasound flow evaluation in neurosurgery include spectral Doppler, power Doppler (PD), and color-Doppler imaging (CDI). These methods have previously been used to investigate the hemodynamics in intracranial aneurysms, AVMs and tumors [4–11]. The CDI and PD modalities both show the presence of blood flow in a region of interest and provide a visual assessment of blood flow. The CDI modality also provides 1-D Doppler measurements of the mean blood velocity and direction. Spectral Doppler methods can further provide a visualization of the full velocity spectrum within a small region of interest. Two-dimensional, contrast-enhanced, B-mode imaging has also been proposed for evaluating flow conditions in cerebral aneurysms [12]. Furthermore, ultrasound transit-time flow measurements have been used to assess flow in neurovascular surgery, but require that the vessel of interest has been dissected so that a probe clamp can be placed around it [13].

Ideally the surgeon would prefer to work in a navigation scene that portrays 3-D vessel geometry as well as flow velocity and direction. However, conventional Doppler-based ultrasound modalities are inherently limited by an angle-dependency in that it only provides a measurement of the flow velocity parallel to the ultrasound

beam axis. Further, the measurable velocity scale is limited, and the imaging system must typically be set to image either low or high velocities present during the cardiac cycle. Detailed 3-D information of flow direction and velocity is for these reasons not currently available, but could provide important clinical information when making key decisions during an operation.

In this work we aim to correct for these limitations by using a model-based approach, where 3-D vessel models generated based on navigated 3-D freehand scanning is used as *a priori* information of vessel geometry and orientation at each scan plane. Having this information ideally allows for angle and aliasing correction, and adds potential for increasing the accuracy and usefulness of a 3-D color-Doppler imaging modality. A similar approach was previously briefly described and patented in the 90s [14], aiming at estimating volume flow in cardiovascular imaging. But to the author's knowledge the topic has not been further pursued and described in the literature. This might be related to inaccuracies in legacy navigation equipment and 3-D modeling approaches, challenges related to the relative motion between the imaging transducer and object, and the relatively high pulsatility of flow in central vessels. To our advantage, the intraoperative context is more suited for such an approach, where the patient is stabilized under sedation, and the flow of interest is more well behaved. Further, although accurate volume flow estimates are desired, more reliable information of 3-D flow direction and velocities may itself provide important clinical information in such a setting, as will be further described.

This paper has been organized as follows. In Section II, the background and methodology is presented. In Section III, *in vitro* experiments using a vessel tree model is used to quantify the accuracy of the approach under varying conditions. Further, *in vivo* examples demonstrating the method used to image an intracranial aneurysm and an AVM is presented. Results and potential future work are discussed in Section IV. In Section V conclusions are presented.

3.2 Methods

3.2.1 Experimental setup, acquisition and pre-processing

The experimental setup used in the laboratory and in the operating room is shown in Fig. 3.1. The system consists of a computer for image processing and navigation, running an in-house software called CustusX (SINTEF Medical technology, Health Research, Trondheim, Norway), connected to an optical 3-D position tracker (NDI Polaris Spectra; Northern Digital, Waterloo, Canada). The accuracy (RMS error) of the position tracker is reported by the manufacturer to be 0.25 mm, however, due to calibration uncertainties the average error of the system has been measured to be 1.4 mm [15]. This calibration error is not a stochastic error, but mainly a constant spatial offset. To acquire ultrasound images, we used a GE Vingmed Vivid 7 ultrasound scanner with a GE M12L linear array transducer and a GE Vingmed E9 ultrasound scanner with a GE 11L linear array transducer (GE Vingmed Ultrasound, Horten, Norway). A direct link between the ultrasound scanner and the

navigation computer provided the in-house navigation system with real-time ultrasound data as video-grabbed images, as seen in Fig. 3.2. This made it possible to make a 3-D model of the vessels on the fly in the operating room. However, to generate a 3-D model with information about flow direction and velocity currently requires raw ultrasound data from the scanner. This currently requires offline processing of stored ultrasound and navigation data, as described in the following sections:

- 1) 3-D ultrasound data were obtained by continuous free-hand 3-D scanning, where the position and orientation of the image planes were stored during acquisition. During the acquisition, demodulated in-phase and quadrature data (IQ-data) were acquired and high-pass filtered to isolate the signal from moving blood. From the filtered IQ-data the autocorrelation data with lag, l , were estimated as described in [16]:

$$R(l) = \frac{1}{M-l} \sum_{k=1}^{M-l} z(k+l)z(k)^*, \quad (3.1)$$

where z is the IQ-data ensemble from one point in the 2-D frame and z^* is the complex conjugate of z . The sum is over the ensemble of pulse emissions (ensemble size), M . The power of the backscattered signal is estimated from $R(0)$, while the velocity along the ultrasound beam axis is estimated as

$$v = \frac{\angle R(1)}{\pi} \cdot v_{\text{Nyq}}. \quad (3.2)$$

Where \angle is the complex phase angle and

$$v_{\text{Nyq}} = \frac{c \cdot PRF}{4f_0}. \quad (3.3)$$

Here c is the speed of sound in blood (1560m/s), PRF is the Doppler pulse repetition frequency and f_0 is the received pulse center frequency.

- 2) Segmentation of blood vessels in the 2-D planes were done by thresholding the velocity and the power of the signal. The thresholds were empirically adapted to the clinical application.
- 3) In conventional color flow imaging the velocity estimates are typically averaged over a fixed number of autocorrelation data frames. The navigation data makes it possible to dynamically set the number of frames to average, in order to avoid smearing out the 2-D images and hence the 3-D reconstructed geometries. This was done by limiting the number of averaging frames when the probe is moved substantially.

After acquisition of the data a 3-D vessel model was reconstructed from registered 2-D color flow images based on optical tracking of the 2-D images. The 3-D reconstruction was done by a Pixel Nearest Neighbor algorithm as described in [17]. We further extracted the vessel centerlines from the segmented model using

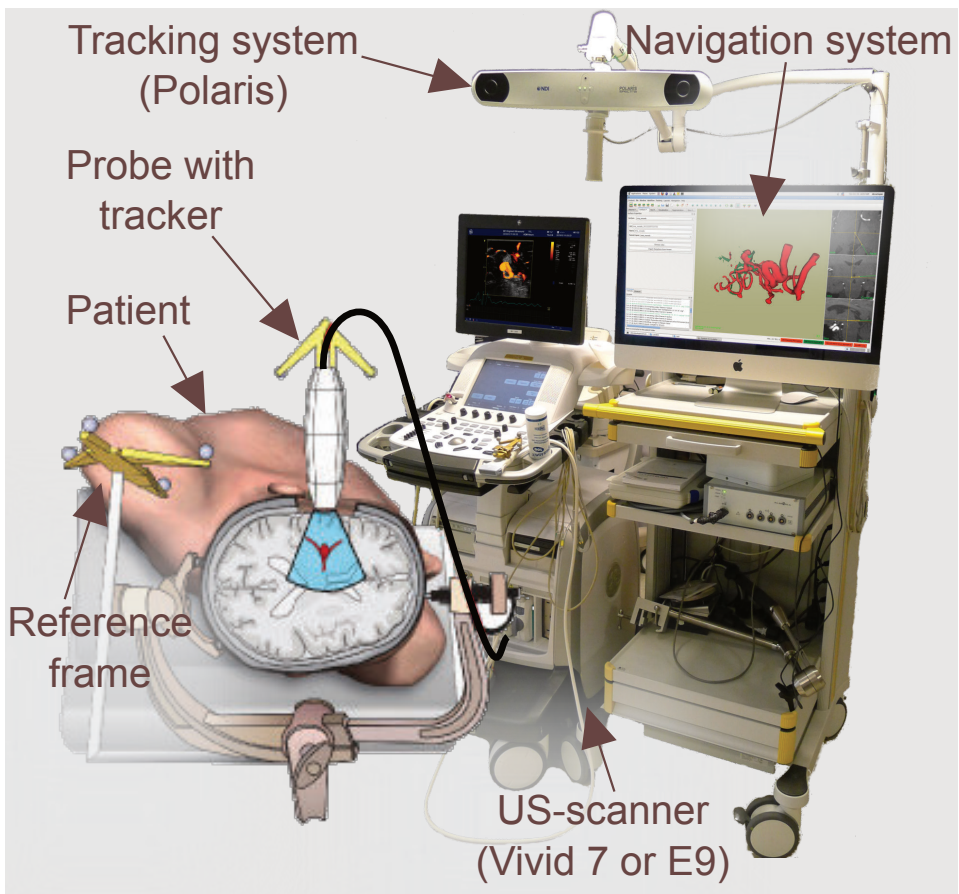


Figure 3.1: The experimental setup used in the operating room and in the laboratory, showing the tracking system, the ultrasound scanner and the navigation system (CustusX). Tracking frames were attached to the patient bench and the ultrasound probes.

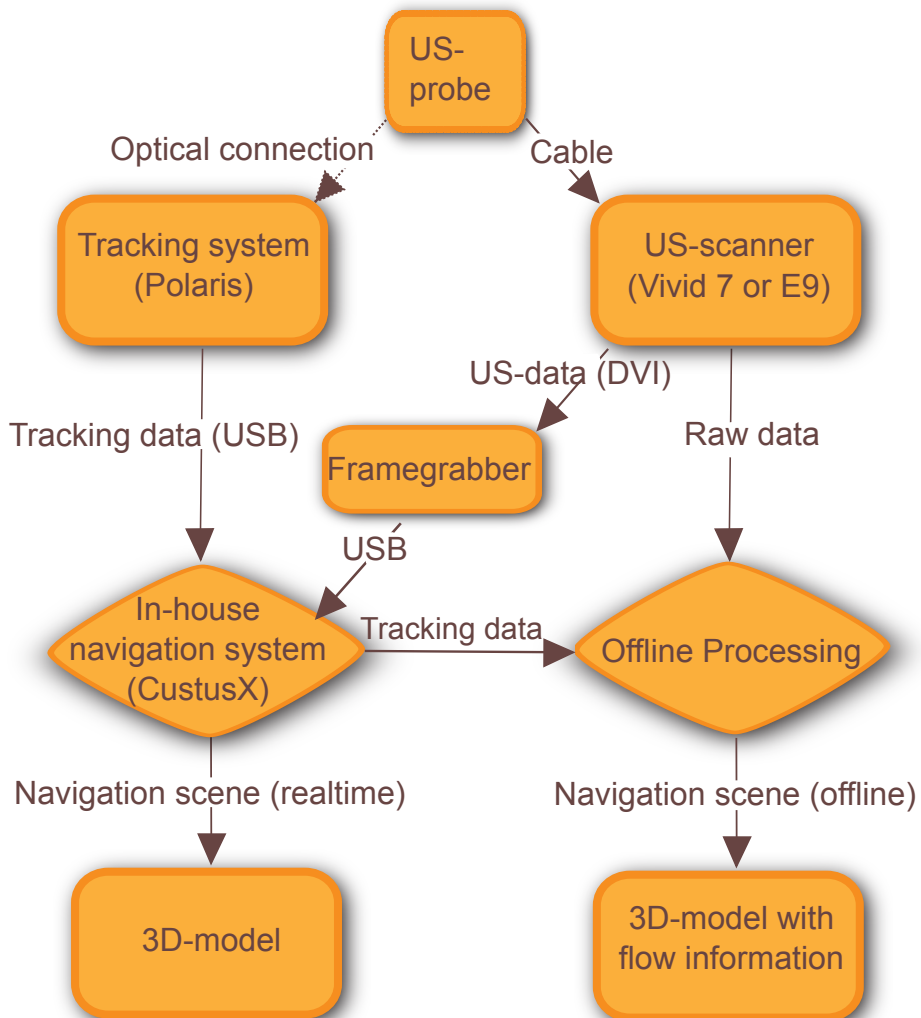


Figure 3.2: Block diagram of the main connections between the systems used. Both the real time processing and offline processing branches are shown.

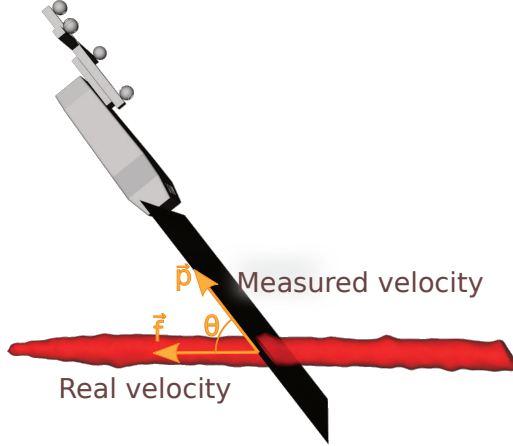


Figure 3.3: An illustration of the 3-D angle-correction procedure, where the estimated angle between the 3-D model and the ultrasound image plane is used to estimate the mean blood velocity of a vessel segment.

a 3-D thinning algorithm [18]. This algorithm results in a point cloud. To link the centerline points, manual seed points were selected, and center line points were linked in a nearest neighboring fashion. Spline interpolation was finally used to get a smooth centerline representation.

3.2.2 Model-based correction of Doppler measurements.

- 1) **Angle estimation.** The vessel centerlines are used as *a priori* information of the vessel orientation. Combined with the registered orientation of each 2-D image plane, the angle, θ , between the true velocity and the measured velocity for measurement j was calculated as:

$$\cos \theta_j = \frac{\vec{f}_j \cdot \vec{p}_j}{\|\vec{f}_j\|_2 \|\vec{p}_j\|_2}, \quad (3.4)$$

where \vec{f}_j is a vector describing the flow direction and \vec{p}_j describes the direction of the velocity measurement, as illustrated in Fig. 3.3. Here \cdot denotes the scalar product of the two vectors and $\|\cdot\|_2$ denotes the Euclidean norm of the vector.

- 2) **Flow direction estimation.** To estimate the flow direction, \hat{d} , in a vessel segment, we assume that less than half of the velocity measurements (pixels) are aliased for most of the frames. The flow direction is estimated as

$$\hat{d} = \frac{1}{\sum_{i=1}^N W_i} \sum_{j=1}^N W_j \frac{v_{\text{Measured},j} \cos(\theta_j)}{|v_{\text{Measured},j} \cos(\theta_j)|}, \quad (3.5)$$

where $|\cdot|$ is the absolute value, j denotes measurement number j , the sum is over all, N , measurements in a vessel segment and W_j is a weight function. The weight function is chosen to prioritize measurements without aliasing and put less emphasis on angles close to 90° . It was chosen as:

$$W_j = A \cdot \left(\frac{\#P_j - \#N_j}{\#P_j + \#N_j} \right)^2 + \begin{cases} 0, & |\cos(\theta_j)| < a \\ 0, & |\cos(\theta_j)| > b \\ 1, & \text{Otherwise} \end{cases} \quad (3.6)$$

where $\#P$ and $\#N$ is the number of positive and negative velocities in cross-section number j . The weight function is chosen to give a low weight to cross-sections with a equal number of positive and negative velocities, which is assumed to be caused by aliasing. The second part weight the measurement with an angle θ , close to 90° less, since the uncertainty at near perpendicular beam-to-flow angles are higher. Also measurements where the angle is close to 0° or 180° get a lower weight, since these measurements are more likely to be aliased. In the following case studies we have set $A = 10$ to prioritize measurements without aliasing. To weight measurements with estimated angles between $26^\circ < \hat{\theta} < 86^\circ$ and $94^\circ < \hat{\theta} < 154^\circ$ most, we have set $a = 0.07$ and $b = 0.9$. The weight function as a function of $\#P$ and the angle, θ , is displayed in Fig. 3.4.

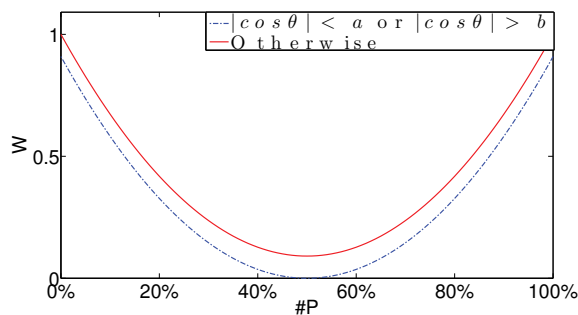


Figure 3.4: The normalized weight, W , as a function of positive measurements, $\#P$ in percent, for different angles, θ . A cross-section with 50% positive and 50% negative velocity measurements, are weighted low since it is assumed to be influenced by aliasing.

The direction estimates have values in the range from -1 to 1. The sign indicates the flow direction, and the absolute value indicates the uncertainty of the estimation. $\hat{d} = \pm 1$ means all measurements indicate the same direction, and if $\hat{d} \approx 0$ the uncertainty is very high and no direction can be predicted.

- 3) **Aliasing correction.** For Doppler-based velocity measurements the axial velocity range is given by v_{Nyq} . Based on the estimated flow direction it is possible to correct

the aliased velocity measurements as

$$\tilde{v}_{k,j} = \begin{cases} 2v_{\text{Nyq}} + v_{k,j}, & \text{for } v_{k,j} < 0, \text{ sign}(\hat{d}) = \text{sign}(\cos \theta_j) \\ -2v_{\text{Nyq}} + v_{k,j}, & \text{for } v_{k,j} > 0, \text{ sign}(\hat{d}) \neq \text{sign}(\cos \theta_j) \\ v_{k,j} & , \text{ else (no aliasing)} \end{cases} \quad (3.7)$$

Where v_k is Doppler measurement k in cross-section number j . Note that this requires a correct estimate of the direction. This will increase the maximum velocity to approximately 2 times v_{Nyq} .

- 4) **Angle correction.** Angle correction of the Doppler measurements is given as

$$\hat{v}_{\text{Real},j} = \frac{\tilde{v}_{\text{Measured},j}}{\cos(\theta_j)}. \quad (3.8)$$

$\tilde{v}_{\text{Measured},j}$ is an average over the vessel cross-section of the aliased corrected Doppler measurements, $\tilde{v}_{k,j}$. As seen for the *in vitro* example in the next section the estimated velocity will be sensitive for angles close to 90° .

It is also of interest to estimate the mean velocity per vessel segment. We then used a linear model $v_{\text{Measured},j} = \hat{v}_{\text{Real}} \cos \theta_j + \epsilon_j$, where ϵ_j is an additive error term. This approach reduces the influence of near perpendicular beam-to-flow angles, hence the estimated velocity will be more robust. Using least squares fitting the estimated velocity for a vessel segment is given by

$$\begin{aligned} \hat{v}_{\text{Real}} &= \underset{v_{\text{Real}}}{\operatorname{argmin}} \sum_{i=1}^N \epsilon_i^2 \\ &= \underset{v_{\text{Real}}}{\operatorname{argmin}} \sum_{i=1}^N (\tilde{v}_{\text{Measured},j} - v_{\text{Real}} \cos \theta_j)^2 \\ &= \frac{\sum_{i=1}^N \tilde{v}_{\text{Measured},j} \cos \theta_j}{\sum_{i=1}^N \cos^2 \theta_j}. \end{aligned} \quad (3.9)$$

The sum is over all measurements with $\hat{\theta} < 70^\circ$ to avoid near perpendicular beam-to-flow angles. The method assumes constant velocity in the vessel segment.

- 5) **Visualization.** To visualize the velocity, the estimated velocity values are mapped to the 3-D mesh of the blood vessels. We have studied two different ways of visualizing the velocity. In one approach we visualized the mean velocity over the whole vessel segment as given by Eqn. (3.9). In a second approach we visualized the mean velocity at each scan plane given by Eqn. (3.8). In this case the velocity may vary along the vessel segments according to the cardiac cycle and also somewhat due to varying beam-to-flow angles. We do not visualize velocities where the measurement uncertainty is high, i.e. where an insufficient number of image planes are at acceptable beam-to-vessel angles. The direction estimate was much more robust and therefore typically shown for larger parts of the vessel structures.

3.2.3 In vitro validation

To validate the estimated flow directions and velocities, an *in vitro* model was constructed to mimic the complex vascular architecture in the brain. The tubes are made of silicone, with higher attenuation than tissue, but immersed in water, with lower attenuation than tissue. A low transmit power was used to obtain a realistic signal-to-noise ratio. An illustration of the *in vitro* setup is shown in Fig. 3.5. Two infusion pumps were used to control flow in two different tubes in the phantom. The liquid used to simulate blood is a mixture of Orgasol (polymers with similar size as red blood cells) and water. The tube inner diameter was 0.9 mm and the blood velocity was set to 7.0 cm/s and 4.4 cm/s for the two tubes respectively.

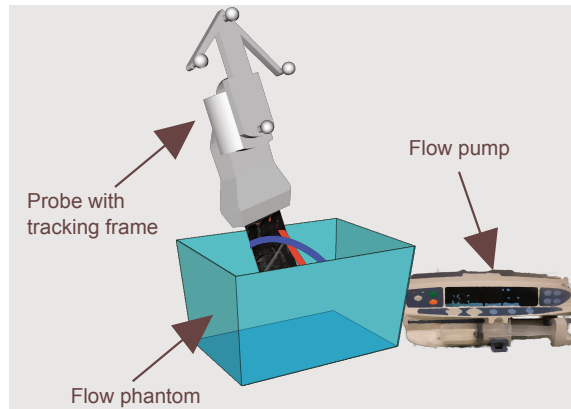


Figure 3.5: The *in vitro* setup used to validate the approach, where two different flows marked in red and blue were generated using two different infusion pumps with known stationary flow.

IQ data were recorded with the ultrasound scanner (Vivid 7) with pulse center frequency set to 7.9 MHz, PRF to 1.5 kHz, an ensemble size of 12 and a sample volume of 0.65 mm. Conventional color flow imaging (CFI) processing was further done offline using a second order polynomial regression filter to attenuate stationary clutter [19], which had a -3 dB filter cut off of 1.5 cm/s.

To verify the aliasing correction approach, a separate *in vitro* setup was used consisting of a straight tube with inner diameter 6 mm, this time imaged using a Vivid E9 ultrasound scanner with a 11L probe. A straight-tube phantom was chosen to easily get a high range of flow-to-beam angles. The tubes are immersed in a material with similar properties as tissue, so a normal transmit power was used. The blood flow was stationary, with a mean velocity of 15.1 cm/s. Due to variation in flow velocity over the cross-section and the variation in angle of insonification, the radial velocities varied from about -20 cm/s to 20 cm/s during acquisition. The clutter filter cut off was 1.9 cm/s, the pulse center frequency was 5.9 MHz and the PRF was set to 2 kHz. The sample volume was 1.0 mm.

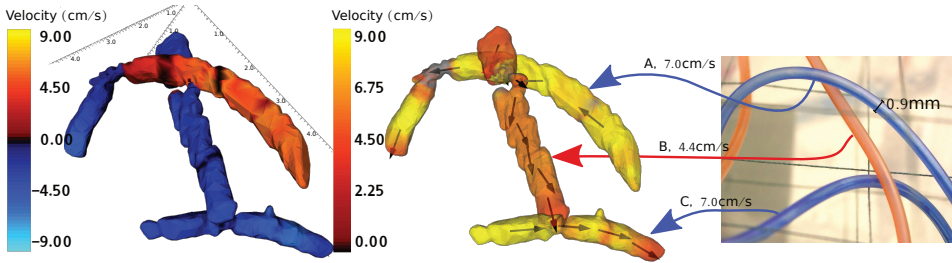


Figure 3.6: *In vitro* results before (left) and after (middle) 3-D angle-correction of axial Doppler velocity measurements, axes scaling are in millimeters. The colorbars indicate the axial velocity (left) and velocity magnitude (middle) respectively. Gray areas (middle) indicate regions where the beam-to-flow angle is near perpendicular, leading to high uncertain velocity estimates. A reference image of the *in vitro* tubes with two different flowrates is shown to the right. As can be observed, without correction it is difficult to interpret the true 3-D flow directions and velocities.

3.2.4 In vivo examples

In the context of neurovascular surgery both the presence of blood flow, and the flow direction and velocity are of interest. In this study we have focused on data from aneurysm and arteriovenous malformations. An aneurysm is a disorder in which weakness in the wall of an artery or vein causes a ballooning of the blood vessel. Intracranial aneurysms can be treated by clipping the aneurysm with special purpose clips, and it is then important to maintain sufficient blood flow in the distal blood vessels. An arteriovenous malformation (AVM) is an abnormal connection between the arteries and veins in the brain, bypassing the capillary vessel network. AVMs can be treated by embolization in combination with microsurgery, where the larger abnormal feeding vessels (also called feeders) are clipped to reduce the flow in the AVM. In [8] it is shown that navigated ultrasound is useful for identification and clipping of feeders to AVMs. In this case the direction of the blood flow is important, but also the velocity and pulsatility patterns may help discern feeding arteries from draining veins and surrounding vessels. *In vivo* data from aneurysm and AVM surgery were acquired with acquisition parameters given in Tab. 3.1 and processed offline as previously described.

Table 3.1: Parameter settings on the ultrasound scanner.

Operation	Scanner	Center frequency, f_0	PRF
Aneurysm 1	GE Vivid7	7.7MHz	2.5kHz
Aneurysm 2	GE E9	5.9MHz	3.0kHz
AVM	GE E9	5.9MHz	2.0kHz

The ultrasound data were acquired after the bone flap had been temporarily removed from the skull, but before opening of the dura. We used a 1 cm thick standoff of sterile gelatin (SonarAid, Switzerland) to obtain a more optimal distance

between the vessels and the ultrasound probe. The collection of data for the study was approved by the local ethics committee and informed consent to participate in clinical research was given by all patients included in the study.

3.3 Results

3.3.1 In vitro experiments

Angle correction. For the first example without any aliasing the blood velocity estimates before angle correction are shown to the left in Fig. 3.6, where the middle figure displays the angle corrected velocity and the right picture shows the flow phantom. In Tab. 3.2, the resulting bias and standard deviation is shown, calculated after angle-correction using Eqn. (3.8) and (3.9). The estimated flow direction is also given in Tab. 3.2 as a number in the range $[-1,1]$, according to Eqn. (3.5). Notice that vessel A has a drop-out when the velocity is changing from negative to positive in the left of Fig. 3.7. The reason is that the probe is near perpendicular to the flow direction. Vessel A and C were imaged mostly in a short axis view, while vessel B is image with a more long axis view.

Table 3.2: *In vitro* results

	Absolute relative bias $ (v_{\text{True}} - \hat{v})/v_{\text{True}} \cdot 100\%$	Flow direction, \hat{d}	Std. Dev.
Vessel A:	3.7%	-0.96	3.2 cm/s
Vessel B:	9.5%	0.89	2.9 cm/s
Vessel C:	2.4%	-0.97	2.2 cm/s

Aliasing correction. In the second *in vitro* experiment with higher blood velocities most of the frames have partly aliased velocities as shown in Fig. 3.8. However, when the angle, θ , is closer to perpendicular to the flow direction for some of the frames, the radial velocity is lower than the Nyquist velocity, and for these frames the correct radial velocities are measured. As seen in Tab. 3.3, the estimated velocities after aliasing correction and angle correction is close to the real velocities. The reference velocity is calculated as the known volume flow divided by the cross section area. Scatter plots of the velocity estimates at the different steps in the correction process are shown in Fig. 3.7. After aliasing correction, the angle dependency is clearly seen, with only positive velocities for θ less than 90° and only negative velocities for $\theta > 90^\circ$. The 80% velocity range interval of the reference velocity is calculated based on an assumption of a parabolic flow profile. After the angle correction, most of the estimated velocities are located around the reference velocity, but close to 90° the uncertainty is high. Some of the variation in velocity estimates is caused by normal variations in a cross section of a vessel. For stationary flow the velocity changes approximately as a parabolic function over the cross section, with a maximum velocity equal 2 times the average velocity. The estimation of the velocity is shown in Fig. 3.9, where the fitted linear model according to Eqn. (3.9) is shown.

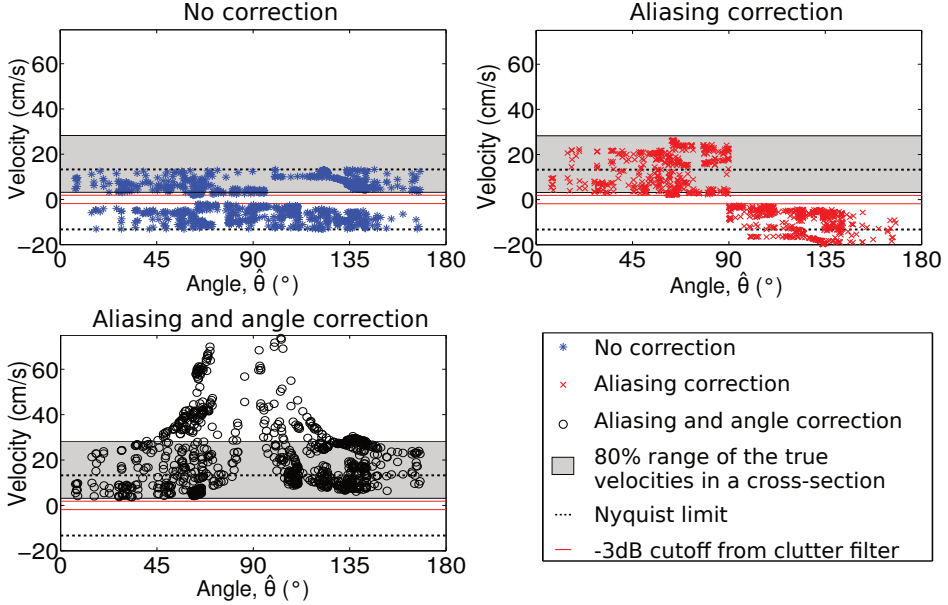


Figure 3.7: *In vitro* result. Showing scatter plots of the estimated velocity at different steps in the correction process: No correction (upper left), after aliasing correction (upper right) and after aliasing and angle correction (lower left). Angle-correction is done by the estimator in Eqn. (3.8), where $\hat{\theta}$ is the estimated beam-to-flow angle. The 80% velocity range interval of the true velocity is calculated based on an assumption of parabolic flow. All the velocity measurements over the cross sections are plotted without any averaging in space or time.

3.3.2 In vivo - intracranial aneurysm and AVM

The directional estimates from two aneurysm operations and one AVM operation is presented in Tab. 3.4. The flow direction is given in range $[-1,1]$, and the different vessels are indicated in figures 3.10, 3.12 and 3.13 respectively.

Aneurysm 1 & 2. In Fig. 3.10, aneurysm 1 is shown before and after angle correction. After angle correction both 3-D directional and velocity information is available. In Fig. 3.11, scatter plots at different correction steps are displayed for aneurysm 2, corresponding to Fig. 3.7 for the *in vitro* trials. The angle and aliased corrected velocities have a variance caused by the uncertainty in the angle estimation. Some of the variation may also be explained by the pulsatility of the blood flow. In Tab. 3.4 the estimated flow direction is given, which was verified by the surgeon during the operation by carefully interpreting the 2-D ultrasound data.

AVM. Different visualizations of the 3-D AVM reconstruction are shown in Fig. 3.13. For this example the velocities in the feeders were so high that there was substantial aliasing with the PRF used. The flow direction was verified by

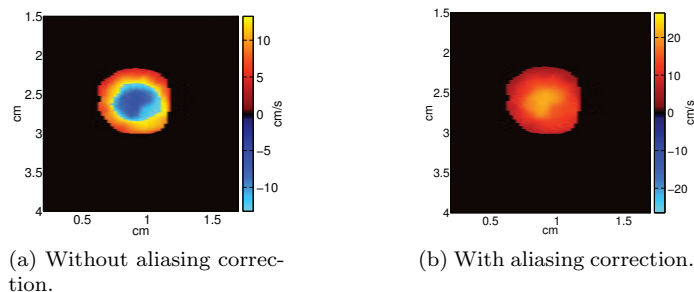


Figure 3.8: 2D-frame of ultrasound data from an *in vitro* experiment. In part of the blood vessel in the left picture the velocity is so high that it folds from positive to negative, observed as "blue" parts in the vessel. There are only positive velocities in the vessel in the right picture, as expected for aliased corrected velocities. Note that there are two different velocity ranges.

Table 3.3: Angle corrected velocity before and after aliasing correction

	Estimated velocity		True velocity	Flow direction, \hat{d}
	Before	After		
Blood vessel A:	3.8cm/s	15.7cm/s	15.1cm/s	0.64

the surgeon during the operation, and the correct direction was found as shown in Tab. 3.4. Based on the estimated flow direction, the velocity measurements were corrected for aliasing. The aliased and angle corrected Doppler measurements are shown in Fig. 3.13. The upper left 3-D model, (a), shows the different velocity estimates along the vessels, estimated by the estimator given in Eqn. (3.8). The lower left 3-D model, (c), shows estimated average velocity as one color for each of the two feeding vessels, estimated by the estimator given in Eqn. (3.9). A microscope picture of the corresponding vessels is also shown (d). The data for the vessels are acquired during about five heart cycles. The time in the heart cycle corresponding to when the velocity measurements are done is shown in Fig. 3.13b. The onset time of systole was set as reference zero time.

3.4 Discussion

In this work we have shown how calibrated 3-D flow images (velocity and direction) can be reconstructed from 2-D ultrasound image slices to provide clinically relevant information not previously available during neurosurgery. The approach is based on 3-D reconstruction and vessel segmentation, where the 3-D geometry and alignment of vessels can be used as *a priori* knowledge for correcting velocity aliasing and angle dependencies in Doppler measurements. The method may for instance help the surgeon to identify feeding vessel of an AVM, and to ensure the correct vessels are clipped before dissection. For an aneurysm operation is it important to

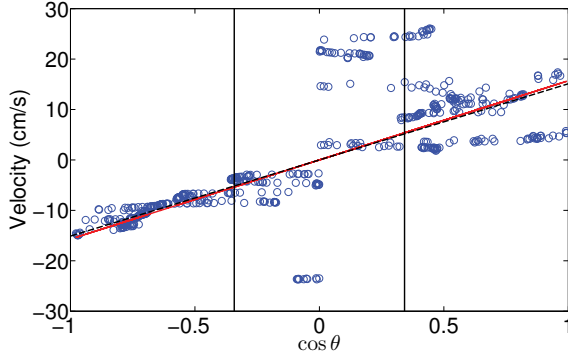


Figure 3.9: *In vitro* result. Estimated angle and aliased corrected velocities averaged over the tube cross-section as a function of $\cos \theta$. The red solid line is the minimum least square fit of the velocities, which gives a estimated velocity of 15.7 cm/s. The black dashed line is the true average velocity, 15.1 cm/s. The vertical lines shows the angle threshold of 70° , steeper angles are not used for estimating the average velocity.

Table 3.4: In vivo results from aneurysm 1, aneurysm 2 and AVM

	Flow directions, \hat{d}
Aneurysm 1. Blood vessel A, B:	0.84, 0.81
Aneurysm 2. Blood vessel A, B, C:	0.97, 0.68, 0.95
AVM 1. Blood vessel A, B:	0.44, 0.61

ensure sufficient blood flow after removing the clips, to avoid unnecessary damage of the brain. Other applications may be to get an improved understanding of the surrounding vessel architecture during tumor resection.

An *in vitro* validation study showed that reasonable accuracy could be obtained for a challenging low-flow imaging scenario. The angle corrected velocities plotted against the estimated angle, as shown in Fig. 3.7, illustrates the limitation of the angle correction for steep angles. For angles steeper than 70° the uncertainty in the velocity is so high, that no angle corrected velocity was shown in the 3-D models. In general, however, the estimation of flow angle proved quite robust. For the second *in vitro* setup with substantial aliasing artifacts, the correct flow direction could still be found, and further used for aliasing correction of the mean velocity. This is important in order to overcome the limited measurable velocity range in color-Doppler imaging.

One method to correct for aliasing was presented in [20], the blood vessel was segmented into regions of positive and negative velocities respectively, and where the smallest segment was assumed to be aliased. In this work we attempted to estimate the flow direction of the blood, and use that information to do aliasing correction. The aliasing correction increases the axial velocity range, i.e. along the ultrasound beam, to $2v_{Nyq}$. In cases where almost all the data are aliased, the

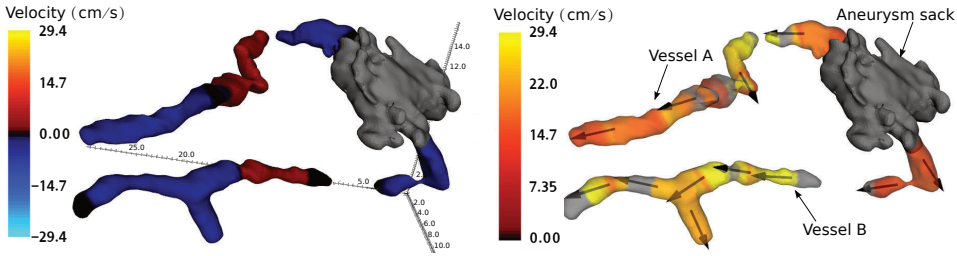


Figure 3.10: *In vivo* results from aneurysm 1. Before (left) and after (right) angle correction of Doppler data from an intracranial aneurysm operation. The color of the 3-D model represents the velocity in beam direction for the left figure. Here it is not possible to interpret the velocity measurements, since the probe orientation is unknown. But in the right figure, where the color represents the angle corrected velocities, meaningful velocity information is shown. The arrows indicate the estimated direction after angle correction. Manually segmentation was done to only show the vessels of interest. The gray color indicate areas with so high uncertainty that the velocity not is shown (angles close to 90°). The Nyquist limit is 13cm/s. The scale of the axes is in millimeter.

estimation of direction will fail and hence also the aliasing correction. We currently require that the ratio between the number of unaliased vs. aliased pixels to be higher than one, for more than 50% of the frames in each vessel segment. When the size of the vessel decreases this measure may become uncertain. Further work should look into the lower limit for this approach. Currently aliasing correction will not be done if the vessel is too small to provide sufficient data.

Further, preliminary *in vivo* trials show promising results. In all the cases the correct flow direction was found. In the feeders of AVMs the velocity can be so high that it is challenging to measure without losing the low velocities of interest. This results in a more uncertain estimation of the flow direction, caused by the higher number of frames with aliased velocities. A higher PRF will increase the Nyquist limit and give less aliasing. Higher PRF will also cause a higher clutter filter cut-off, and vessels with low velocity in beam direction will not be imaged.

Velocity measurements without angle correction, as visualized in Fig. 3.10a, are not possible to interpret in a 3D-model where information about the probe orientation is unknown. But after angle correction, as seen in Fig. 3.10b, meaningful information of the velocity could be obtained.

The accuracy of the angle-correction is dependent on accurate angle estimates, which depends on the accuracy of vessel segmentation, centerline extraction, and position sensor calibration. The estimation of flow direction along vessel segments proved quite robust. However, for near-perpendicular beam-to-flow angles, angle-correction error have a large impact on the estimated velocities. In estimation of the flow direction angles up to 86° were accepted as valid estimates in our examples, while for angle correction of the velocities only angles up to 70° were used. As seen in Fig. 3.12 the variance of the angle corrected velocities increases

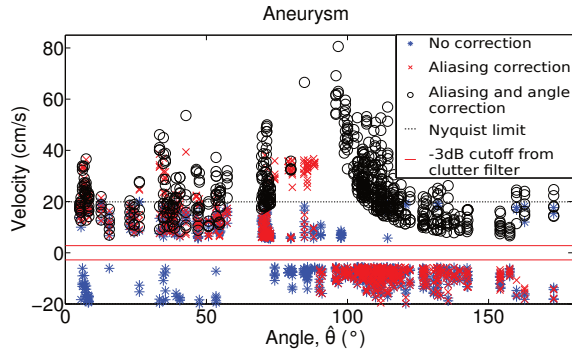


Figure 3.11: *In vivo* results for aneurysm 2, showing a scatter plot of the estimated velocities at different steps in the correction process: No correction, after aliasing correction and after aliasing and angle correction. The angle is the estimated angle, θ , between beam direction and the flow direction. All the velocity measurements over the cross sections are decimated and plotted without any averaging in space or time.

for angles steeper than 70° . This means that more measurements are available for flow direction estimate than for the angle correction of velocities. Consequently the quality for vessels crossing near-perpendicular to the beam direction will be lower than for other vessels. Further, to successfully angle-correct the velocity data the method requires that the image planes are not all near-perpendicular to individual vessel segments. In a clinical setting it is important to only show trustworthy information, therefore the velocities with a high uncertainty were not shown in the final 3-D models. In the example from the AVM operation the majority of angles are in fact steeper than 70° , seen as gray parts in Fig. 3.13a. Here an additional acquisition with the probe tilted a bit more would have given a better angle correction of the velocities. The data of the aneurysm shown in Fig. 3.10 are acquired at more acceptable angles throughout the scan, and angle-corrected velocities are shown for the majority of the vessels.

An estimation of the volume flow will also be of clinical interest. This will require an estimate of the vessel cross-sectional area which may be obtained from the 3-D model. This is focus for further work. A volume flow estimation will be more uncertain than the angle corrected velocities, since the volume flow must be based on both the angle corrected velocity and the estimated cross-sectional area.

Pulsatile flow is one source of error when estimating the mean velocities based on 3-D data obtained from freehand ultrasound acquisitions. The velocities are measured at different states in the heart cycle, leading to variation along the blood vessel as seen in Fig. 3.13a. As expected, it is observed that some of the highest velocities in Fig. 3.13a, marked with I and II, corresponds to the time right after contraction of the heart as seen in Fig. 3.13b. Our aim in this work was to estimate the mean velocity over the cardiac cycle, by averaging over sufficient time to remove the temporal flow variation in each vessel segment. There is uncertainty in

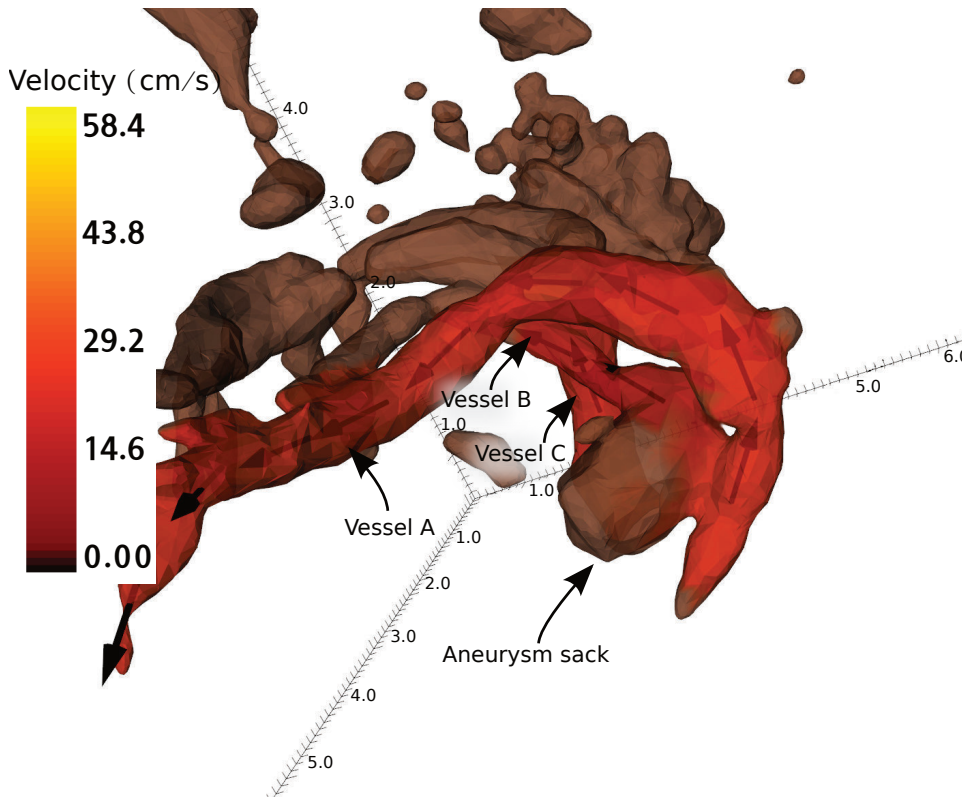


Figure 3.12: *In vivo* results angle correction of Doppler data from the second intracranial aneurysm. The color of the 3-D model represents the angle-corrected velocity. The arrows indicate the estimated direction after angle-correction. The Nyquist limit is 20cm/s. The scale of the axes is in millimeter.

this measurement if either the temporal averaging time is not sufficient, or if the frame rate is too low to capture the complete cardiac cycle variation. Typically, data from several cardiac cycles are included for each vessel segment which helps in this regard. Further, ECG gating could be used to ensure that flow is shown in a particular region of the cardiac cycle on the expense of robustness due to reduced averaging. Future work should investigate the potential pitfalls and possible solutions due to pulsatile flow.

Improved accuracy may be expected for real-time 3-D imaging as more flexible averaging options are available. Real-time 3-D imaging will allow for easier acquisition over several heart cycles, thereby eliminate problems with pulsation and flashing. The acquisition will be easier and the acquisition time will also be reduced.

Using conventional color flow imaging and a wide region of interest compromises frame rate and/or image quality. Our recordings had a frame rate of 10-15 Hz,

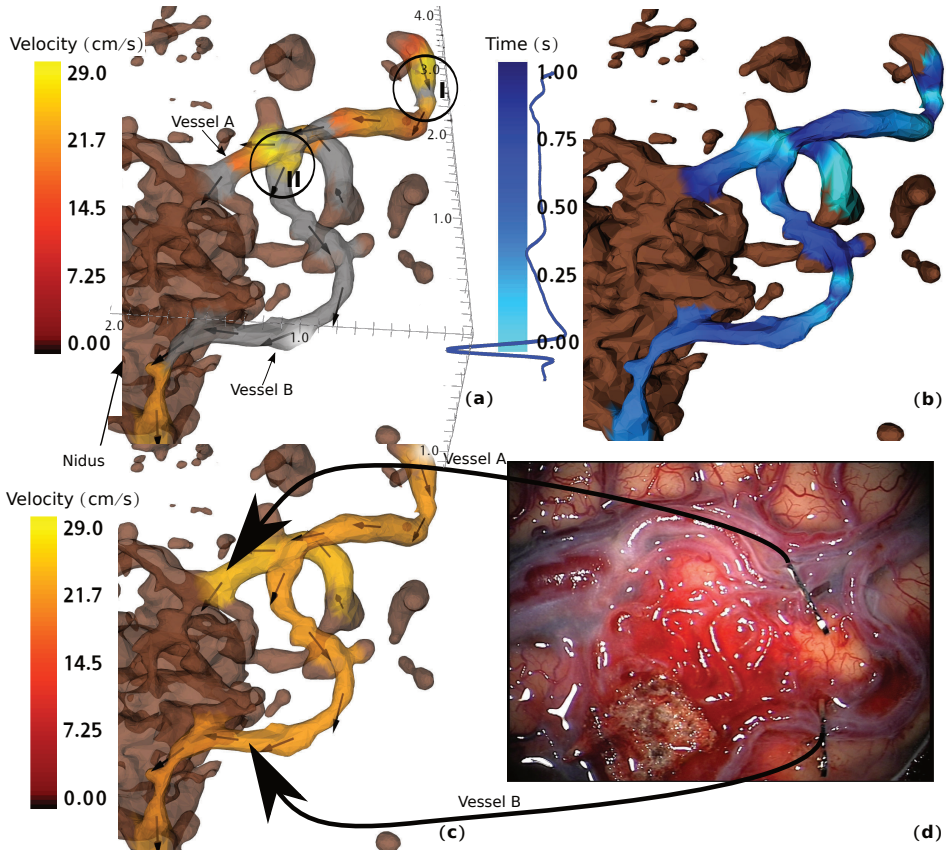


Figure 3.13: *In vivo* results of an arteriovenous malformation (AVM). (a) The upper left 3-D model shows the velocity estimates along the vessels, estimated by the estimator given in Eqn. (3.8). The gray color indicate areas with high uncertainty ($\hat{\theta} > 70^\circ$), hence no velocity estimate is shown. The brown colored regions indicate parts where we are not interested in the flow direction and angle corrected velocities. (b) The color represents the relative time in the heart cycle for when the velocity is measured. (c) The 3-D model shows estimated average velocity as one color for each of the two feeding vessels, estimated by the estimator given in Eqn. (3.9). (d) AVM clips of the feeders seen in the microscope. The Nyquist velocity limit is 13cm/s. The scale of the axes is in millimeter.

resulting in sparse temporal data for the 3-D reconstruction. Due to changes in the data between each frame, our ability to do temporal averaging was limited. Further work will investigate how an acquisition based on parallel receive beamforming can be used to improve this aspect. By transmitting an unfocused and wide ultrasound beam, a larger region can be covered by one transmission, and multiple image lines can be generated in parallel. This results in higher frame rate than in conventional CFI. Parallel receive beamforming will also allow for using a higher ensemble size to improve wall filtering for better low-flow detection. Parallel receive beamforming, its benefits and limitations, are further described in [21, 22]. In [23] plane wave imaging and parallel receive beamforming was used to provide high quality images of blood vessels in rat brains.

Improved quality of color flow images by using contrast agents has been documented, especially for improving the ability to detect smaller vessels [24]. Contrast may reduce dropouts caused by imaging at near perpendicular angles. So it might improve the quality of the 3-D volume, hence also improve the quality of the angle-correction. Contrast agents will complicate the acquisition since it requires injection of contrast, but it should be a relatively simple addition in intraoperative setting.

The success of the model-based angle correction is dependent on accurate vessel segmentation, and further accurate center line extraction. This can be challenging to achieve in the neurovascular architecture where also small vessels are of interest. In Fig. 3.13a the two vessels partially merge, at the point marked II, due to inadequate spatial resolution. A high uncertainty in the centerline representation will cause a high uncertainty of the angle estimate, $\hat{\theta}$, and hence influence the uncertainty of the angle corrected velocity. The centerline extraction method currently requires a manual step in order to generate a continuous centerline. For instance, in situations where two vessels are overlapping due to the finite resolution of the ultrasound imaging system, manual corrections might be necessary to get a continuous centerline for the correct vessel. Further work should investigate how to further automate this step. Alternatively, a semi-automatic approach based on feedback from the surgeon could be taken in order to pinpoint vessel segments of interest. Also given a successful coregistration, preoperative MR angio images could also be used for the extraction of centerlines.

The method requires some infrastructure in the operating room, but this equipment is currently in use in many operating theaters to day. The ultrasound scanner can be built into a navigation system, hence only one unit will be required [25]. Although indications are given for the usefulness of calibrated 3-D velocity and direction in the neurosurgical context, a larger patient study is needed to properly establish the clinical value of the method and document the robustness of the method for a larger variation of patient cases. This is our main focus for further work.

3.5 Conclusion

By using a model-based approach to angle-correct Doppler measurements, 3-D information about blood velocities and flow direction was provided based on free-hand 3-D ultrasound imaging and position sensor information. The flow directional information could further be used to increase the measurable velocity range in color-Doppler imaging by correcting for velocity aliasing. The estimate of the flow direction proved robust, and was correctly found in all examined cases. *In vitro* experiments further revealed a good accuracy for estimating the angle corrected velocity. However, imaging at near perpendicular angles is currently a limitation. Potential clinical use was demonstrated for neurosurgical applications. However, the approach may also have applications in general cardiovascular imaging where the principal flow direction and velocity is of interest.

REFERENCES

- [1] B. Albayrak, a. F. Samdani, and P. M. Black, “Intra-operative magnetic resonance imaging in neurosurgery,” *Acta neurochirurgica*, vol. 146, no. 6, pp. 543–557, Jun. 2004. [Online]. Available: <http://link.springer.com/10.1007/s00701-004-0229-0><http://www.ncbi.nlm.nih.gov/pubmed/15168222>
- [2] O. M. Rygh, T. A. Nagelhus Hernes, F. Lindseth, T. Selbekk, T. Brostrup Muller, and G. Unsgaard, “Intraoperative navigated 3-dimensional ultrasound angiography in tumor surgery,” *Surgical neurology*, vol. 66, no. 6, pp. 581–592, 2006.
- [3] I. Reinertsen, F. Lindseth, G. Unsgaard, and D. L. Collins, “Clinical validation of vessel-based registration for correction of brain-shift,” *Medical image analysis*, vol. 11, no. 6, pp. 673–684, Dec. 2007. [Online]. Available: <http://linkinghub.elsevier.com/retrieve/pii/S1361841507000679>
- [4] G. Unsgaard, O. Solheim, F. Lindseth, and T. Selbekk, “Intraoperative Imaging with 3D Ultrasound in Neurosurgery,” *Acta Neurochirurgica*, vol. 109, pp. 181—186, 2011. [Online]. Available: <http://www.springerlink.com/index/10.1007/978-3-211-99651-5>
- [5] G. Unsgaard, O. M. Rygh, T. Selbekk, T. B. Müller, F. Kolstad, F. Lindseth, and T. N. Hernes, “Intra-operative 3D ultrasound in neurosurgery,” *Acta neurochirurgica*, vol. 148, no. 3, pp. 235–253, Mar. 2006. [Online]. Available: <http://www.ncbi.nlm.nih.gov/pubmed/16362178>
- [6] J. M. Gilsbach and W. E. Hassler, “Intraoperative Doppler and real time sonography in neurosurgery,” *Neurosurgical review*, vol. 7, no. 2, pp. 199–208, 1984.
- [7] T. Hölscher, J. Rodriguez-Rodriguez, W. G. Wilkening, and J. C. Lasheras, “Intraoperative brain ultrasound: A new approach to study flow dynamics in intracranial aneurysms,” *Ultrasound in Medicine & Biology*, vol. 32, no. 9, pp. 1307–1313, 2006.
- [8] G. Unsgaard, S. Ommedal, O. M. Rygh, and F. Lindseth, “Operation of Arteriovenous Malformations Assisted by Stereoscopic Navigation-controlled Display

- of Preoperative Magnetic Resonance Angiography and Intraoperative Ultrasound Angiography,” *Neurosurgery*, vol. 56, no. Supplement 2, pp. 281–290, Apr. 2005.
- [9] M. Woydt, K. Greiner, J. Perez, A. Krone, and K. Roosen, “Intraoperative color duplex sonography of basal arteries during aneurysm surgery.” *Journal of neuroimaging: official journal of the American Society of Neuroimaging*, vol. 7, no. 4, p. 203, 1997.
- [10] M. Woydt, J. Perez, J. Meixensberger, A. Krone, N. Soerensen, and K. Roosen, “Intra-operative colour-duplex-sonography in the surgical management of cerebral AV-malformations,” *Acta neurochirurgica*, vol. 140, no. 7, pp. 689–698, 1998.
- [11] G. Unsgaard, S. Ommedal, T. Muller, A. Gronningsaeter, and T. a. Nagelhus Hernes, “Neuronavigation by intraoperative three-dimensional ultrasound: initial experience during brain tumor resection.” *Neurosurgery*, vol. 50, no. 4, pp. 804–12; discussion 812, Apr. 2002. [Online]. Available: <http://www.ncbi.nlm.nih.gov/pubmed/11904032>
- [12] G. Cantón, D. I. Levy, and J. C. Lasheras, “Hemodynamic changes due to stent placement in bifurcating intracranial aneurysms,” *Journal of neurosurgery*, vol. 103, no. 1, pp. 146–155, 2005.
- [13] S. Amin-Hanjani, G. Meglio, R. Gatto, A. Bauer, and F. T. Charbel, “The utility of intraoperative blood flow measurement during aneurysm surgery using an ultrasonic perivascular flow probe,” *Neurosurgery*, vol. 58, no. 4, p. ONS, 2006.
- [14] D. Adam, K. Kempner, M. Vivino, E. Tucker, and M. Jones, “Cardiovascular flow velocity measurements by 2D Doppler imaging for assessment of vascular function.” *Advances in experimental medicine and biology*, vol. 346, p. 393, 1993. [Online]. Available: <http://www.ncbi.nlm.nih.gov/pubmed/8184780>
- [15] F. Lindseth, T. Langø, J. Bang, and T. N. Hernes, “Accuracy evaluation of a 3D ultrasound-based neuronavigation system.” *Computer aided surgery : official journal of the International Society for Computer Aided Surgery*, vol. 7, no. 4, pp. 197–222, Jan. 2002. [Online]. Available: <http://www.ncbi.nlm.nih.gov/pubmed/12454892>
- [16] C. Kasai, K. Namekawa, A. Koyano, and R. Omoto, “Real-time two-dimensional blood flow imaging using an autocorrelation technique,” *IEEE Trans. Sonics Ultrason*, vol. 32, no. 3, pp. 458–464, 1985. [Online]. Available: http://server.elektro.dtu.dk/personal/jaj/31545/documents/kasai_et_al_1985.pdf
- [17] O. V. Solberg, F. Lindseth, H. Torp, R. E. Blake, and T. a. Nagelhus Hernes, “Freehand 3D ultrasound reconstruction algorithms—a review.” *Ultrasound in medicine & biology*, vol. 33, no. 7, pp. 991–1009, Jul. 2007. [Online]. Available: <http://www.ncbi.nlm.nih.gov/pubmed/17512655>

REFERENCES

- [18] T. Lee and R. Kashyap, "Building skeleton models via 3-D medial surface/axis thinning algorithms," *CVGIP: Graphical Model and Image*, 1994.
- [19] S. Bjærum, H. Torp, and K. Kristoffersen, "Clutter Filter Design for Ultrasound Color Flow Imaging," *Ultrasonics, Ferroelectrics and Frequency Control, IEEE Transactions on*, vol. 49, no. 2, pp. 204–216, 2002.
- [20] S. Muth, S. Dort, I. A. Sebag, M.-J. Blais, and D. Garcia, "Unsupervised dealiasing and denoising of color-Doppler data." *Medical image analysis*, vol. 15, no. 4, pp. 577–88, Aug. 2011. [Online]. Available: <http://www.ncbi.nlm.nih.gov/pubmed/21482175>
- [21] D. P. Shattuck, M. D. Weinschenker, S. W. Smith, and O. T. von Ramm, "Explososcan: a parallel processing technique for high speed ultrasound imaging with linear phased arrays." *The Journal of the Acoustical Society of America*, vol. 75, no. 4, pp. 1273–82, Apr. 1984. [Online]. Available: <http://www.ncbi.nlm.nih.gov/pubmed/6725779>
- [22] T. Hergum, T. Bjåstad, K. Kristoffersen, and H. Torp, "Parallel beamforming using synthetic transmit beams." *IEEE transactions on ultrasonics, ferroelectrics, and frequency control*, vol. 54, no. 2, pp. 271–80, Feb. 2007. [Online]. Available: <http://www.ncbi.nlm.nih.gov/pubmed/21384334>
- [23] E. Macé, G. Montaldo, I. Cohen, M. Baulac, M. Fink, and M. Tanter, "Functional ultrasound imaging of the brain." *Nature Methods*, vol. 8, no. 8, pp. 662–664, Jul. 2011. [Online]. Available: <http://www.nature.com/doi/10.1038/nmeth.1641>
- [24] B. B. Goldberg, J. B. Liu, and F. Forsberg, "Ultrasound contrast agents: a review." *Ultrasound in medicine & biology*, vol. 20, no. 4, pp. 319–33, Jan. 1994. [Online]. Available: <http://www.ncbi.nlm.nih.gov/pubmed/22161614>
- [25] A. Gronningsaeter, A. Kleven, S. Ommedal, T. E. Aarseth, T. Lie, F. Lindseth, T. Langø, and G. Unsgaard, "SonoWand, an ultrasound-based neuronavigation system," *Neurosurgery*, vol. 47, no. 6, p. 1373, 2000.
- [26] E. Birngruber, R. Donner, and G. Langs, "matVTK - 3D visualization for Matlab," in *Proceedings of the MICCAI 2009 Workshop on systems and architectures for CAI*, 2009.

Chapter 4

Improved quality of freehand 3-D ultrasound color flow imaging by multi-angle compounding

Daniel Høyer Iversen^{1,2}, Frank Lindseth^{2,3}, Geirmund Unsgaard⁴, Hans Torp¹ and Lasse Lovstakken¹

¹MI Lab and Dept. of Circulation and Medical Imaging, Norwegian University of Science and Technology, Trondheim, Norway

²SINTEF Medical Technology, Trondheim, Norway

³Department of Computer and Information Science, Norwegian University of Science and Technology, Trondheim, Norway

⁴Department of Neurosurgery, Trondheim University Hospital, Norway

Abstract — 3-D imaging of blood flow based on 2-D ultrasound scanning and position sensor information can be used to portray clinical information not currently available in vascular and peripheral imaging. During surgery, information of blood flow is important to identify and avoid damage to important vessels. 3-D intraoperative ultrasound flow imaging has proven useful in this respect. However, due to Doppler angle-dependencies and the complexity of the vascular architecture, the generated 3-D image of blood vessels often have drop-outs in the vessel structure. In this work we aim to reduce the number of drop-outs in the 3-D blood flow images by combining 2-D flow images with different transmit angles.

The compounded 2-D images are further reconstructed to a 3-D flow image based on information from an accurate position sensor system. The method was implemented on a research ultrasound scanner for real-time processing of the data, and in vitro trials showed promising results. The method also showed promising results in vivo using a clinical approved high-end scanner, improving the 3-D image quality of the feeding arteries of an arteriovenous malformation.

4.1 Introduction

Ultrasound color flow imaging has an established and important role in diagnosis of cardiovascular disease. Currently, a 3-D probe suited for vascular imaging is not available. 3-D reconstruction of flow based on 2-D scanning and position sensor information can, however, be used to portray clinical information not currently available in vascular and peripheral imaging. A high quality 3-D image of blood flow provides an intuitive presentation of the geometry of the blood vessels. While quantitative measurements such as 3-D velocity information and volume flow is considered be clinical useful.

Ultrasound flow imaging has some artifacts and limitations that compromise the image quality. For instance, the range of measurable velocities is frequently insufficient for capturing both the low and high flow velocities. The lower velocity limit regarding detection of blood flow is in practice determined by the clutter filter cut-off and the angle between the beam axis and the flow direction.

Due to the potentially complex nature of these vascular architecture, the flow direction can be close to perpendicular to the beam direction for some parts of the blood vessels. This will cause a low axial velocity in the beam direction and then a signal drop-out in the acquired 2-D image. In reconstructed 3-D images, complete drop-outs or thinning of the vessel model will occur, and for a complex vascular network it can be difficult to interpret the resulting 3-D model.

3-D reconstruction of flow has proven useful for intraoperative imaging, where high quality flow 3-D images are especially important. During a surgical procedure the flow conditions might change, and intraoperative flow imaging can be important to get updated information about blood flow and vessel structures. Navigated 3-D freehand ultrasound color flow imaging has previously proven useful to obtain 3-D images of vessels during surgery [1]. However, current limitations in color flow imaging complicates interpretation and an improved image quality will in general increase the diagnostic certainty. Ideally the surgeon would prefer to work in a navigation scene that portrays 3-D vessel geometry and flow velocity. However, this is challenging due to pulsative flow, a complex architecture, a wide span of blood velocities and often small dimension of the blood vessels.

For instance in neurosurgery, information about the blood vessel structure can be important to avoid damage to vessels during tumor resection, to identify the feeding arteries of arteriovenous malformations (AVMs), and is advantageous when identifying and securing flow in the distal branches of intracranial aneurysms af-

ter clipping. Intraoperative 3-D ultrasound imaging is a cost and time efficient modality that has proven useful for providing updated information about the vessel structures and blood flow during the surgery.

Previous work has studied how contrast agents can improve the quality of color flow images, especially for improving the ability to detect smaller vessels [2]. Contrast may also reduce drop-outs caused by imaging at near perpendicular angles, and may therefore also improve the quality of the 3-D volume. Contrast agents will, however, complicate the acquisition since it requires intravenous injection of contrast agent.

Compounding of B-mode images has been investigated for several years. Such a modality could provide a higher quality image and reduce the image noise. In this study we will use the technique from B-mode compounding to obtain higher quality 3-D images of blood vessels.

In this work we aim to improve the quality of vascular 3-D images, by compounding of Doppler 2-D images with different transmit angles to reduce the number of drop-outs. The 3-D vessel model is generated based on navigated 3-D free-hand scanning, where the position and orientation of the probe is registered by an optical sensor. This approach can be used to improve 3-D flow imaging in general vascular and peripheral imaging where 2-D matrix array probes are currently unavailable, and may have particular use in intraoperative settings where imaging conditions are stable, and where the use of navigation equipment is more readily available in current practise [1].

This paper has been organized as follows. In Section II, the background and methodology is presented. In Section III, *in vitro* experiments is used to validate the method. Further, *in vivo* examples demonstrating the method used to image the radial artery of a healthy volunteer and an intracranial arteriovenous malformation. Results and potential future work are discussed in Section IV. In Section V conclusions are presented.

4.2 Methods

4.2.1 Compounding of color flow data

The axial velocity range in CFI is determined by the imaging setup and the clutter filter design. The maximum measurable velocity, given from the Nyquist sampling theorem, can be expressed as

$$v_{\text{Nyq}} = \frac{c \cdot \text{PRF}}{4f_0}. \quad (4.1)$$

Here c is the speed of sound in blood (1560m/s), PRF is the Doppler pulse repetition frequency and f_0 is the received pulse center frequency.

The lower limit regarding detection and estimation of blood velocities in the beam direction is in practice determined by the clutter filter properties, as given by the filter frequency response characteristics such as transition region steepness

and stop band attenuation. For a polynomial regression filter as used in this work, the -3dB cut-off velocity in the probe direction is given in [4] as

$$v_{-3\text{dB}} \approx 0.42 \cdot \frac{N+1}{M} \cdot 2v_{\text{Nyq}}. \quad (4.2)$$

Here N is the filter order of the polynomial regression filter and M is the number of pulse emissions (ensemble size). The minimum detectable blood flow velocity in the flow direction will then be

$$v_{\text{min}} = \frac{v_{-3\text{dB}}}{\cos(\theta)}, \quad (4.3)$$

where θ is the angle between the flow direction and the beam direction. The minimum detectable blood flow velocity in the flow direction increases as the angle θ increases.

In Fig. 4.1 color flow images for three different transmit angles are shown. The blue color represents flow away from the probe and red color represents flow towards the probe, hence the blood is here flowing from left to right in the images. When the color change from blue to red there is a part where the flow velocity in the beam direction is below the lower limit of detectable velocities, v_{min} . In these parts, called drop-outs, no velocity information is available. As can be observed, these drop-outs occur in three different places for the three different transmit angles. By averaging or finding the maximum signal power over the different transmit angles the images can be combined to one image with reduced drop-outs.

To ensure sufficient signal from all parts of the blood vessel a high steering angle can be required. A too high steering angle of the transmit beam will give unwanted interference, called grating lobes. Grating lobes may infer visible image artifacts, and degrade the contrast resolution as for beam sidelobes. The angle, θ_g between the grating lobes and the mainlobe is determined by the size of the individual array elements, called the pitch, p . The angle to the first grating lobe is given as

$$\theta_g = \pm \arcsin\left(\frac{c}{f \cdot p}\right), \quad (4.4)$$

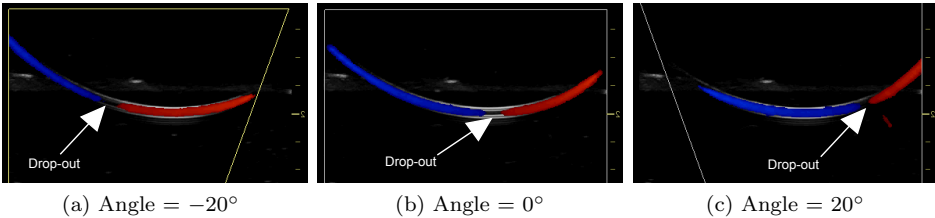


Figure 4.1: A demonstration of the angle-dependency in color flow imaging based on three images with different steering angles. Blue color represents flow away from the beam direction and red color represents flow to probe, so the blood is here flowing from left to right in the images. A drop-out is seen where the flow direction is near perpendicular to the beam direction.

where c is the speed of sound in human tissue (1540m/s) and f is the frequency of the signal. So smaller probe elements allows larger steering angles without getting disturbance from grating lobes [5].

4.2.2 Position sensor setup

The experimental setup used for data recordings is shown in Fig. 4.2. The system consists of a computer for image processing and navigation, running an in-house software called CustusX (SINTEF Medical technology, Health Research, Trondheim, Norway) [6], connected to an optical 3-D position tracker (NDI Polaris Spectra; Northern Digital, Waterloo, Canada). The accuracy (RMS error) of the position tracker is reported by the manufacturer to be 0.25 mm, however, due to calibration uncertainties the average error of the system has been measured to be 1.4 mm [7]. This calibration error is not a stochastic error, but mainly a constant spatial offset.

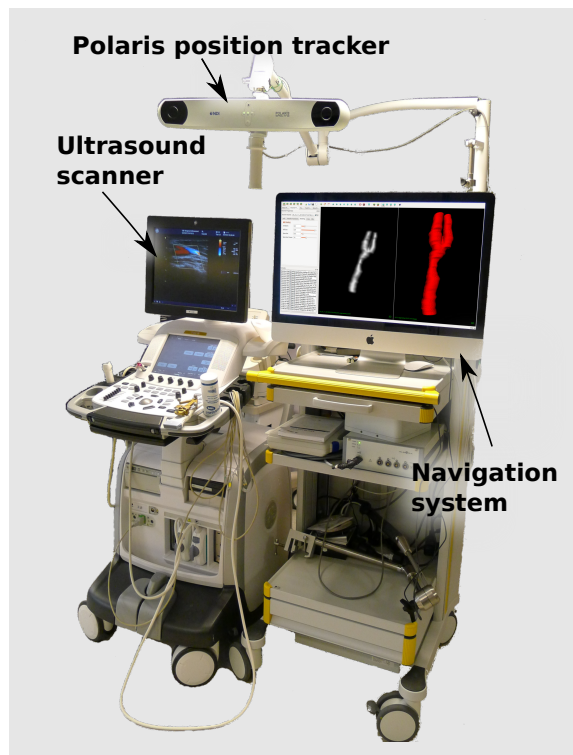


Figure 4.2: The navigation system. Showing the position tracker, the ultrasound scanner and the navigation system. (CustusX).

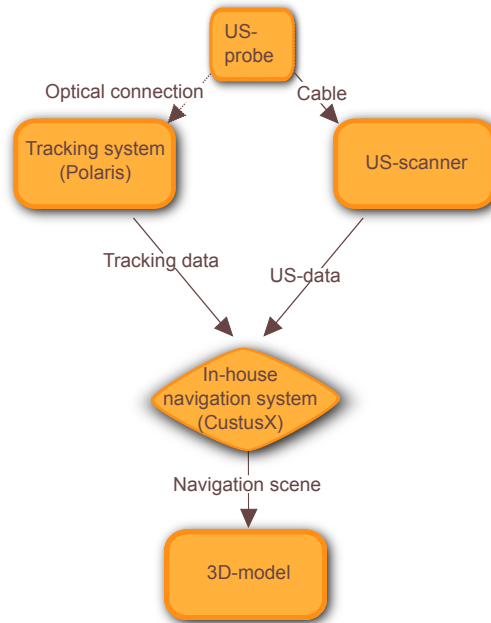


Figure 4.3: Block diagram of the main connections between the systems used.

4.2.3 Real-time implementation

The method for compounding of flow data was implemented on a research scanner, a SonixMDP ultrasound scanner with a 5-14 MHz linear array transducer (Ultrasonix, Richmond, BC, Canada). An application programming interface (API) allows full flexibility in setting up the transmit/receive beams and receive processing.

- 1) 3-D ultrasound data were obtained by continuous free-hand scanning, where the position and orientation of the image planes were stored during acquisition.
- 2) The acquisition setup was implemented using the development toolkit Texo, which allows custom transmit and receive sequences to be created. A setup with three different angles were chosen, and a complete flow image is sequentially made for each angle. The data for each angle is made by merging several lateral image regions acquired subsequently in time. This approach is often termed beam interleaved acquisition, and is used to obtain a given Doppler PRF without affecting the frame rate [8].
- 3) Dynamic receive beamforming was applied with a receive angle equal to the transmit angle.

- 4) The custom beamformed RF data were received from the scanner API and further down-mixed and low-pass filtered to demodulated in-phase and quadrature data (IQ-data).
- 5) The IQ-data were high-pass filtered with a polynomial regression filter to isolate the signal from moving blood [9].
- 6) From the filtered IQ-data the autocorrelation data with lag, l , were estimated as described in [10]:

$$R(l) = \frac{1}{M-l} \sum_{k=1}^{M-l} z(k+l)z(k)^*, \quad (4.5)$$

where z is the IQ-data ensemble from one point in the 2-D frame and z^* is the complex conjugate of z . The sum is over the ensemble of pulse emissions (ensemble size), M . The power of the backscattered signal is estimated from $R(0)$, while the velocity along the ultrasound beam axis is estimated as

$$v = \frac{\angle R(1)}{\pi} \cdot v_{\text{Nyq}}. \quad (4.6)$$

Where \angle is the complex phase angle.

- 7) The final power image, $R(0)$, from the zero angle transmission were displayed in real time at the ultrasound scanner and transmitted to the navigation system as a reference. The transmission was done over the transmission control protocol (TCP) where both the image and geometrical information were sent. At the same time all the data were stored to the disk as IQ data.
- 8) After acquisition of the data a 3-D vessel model was reconstructed from registered 2-D color flow images based optical tracking. The 3-D reconstruction was done by a Pixel Nearest Neighbor algorithm as described in [11]. For comparing the effect of compounding images from different angles, 3-D volumes were reconstructed with only one angle and all three angles from the stored IQ-data for comparison.

4.2.4 In vitro experiments

To validate the method, an *in vitro* model was constructed to mimic a small blood vessel. A tube is made of silicone, with higher attenuation than tissue, but immersed in water, with lower attenuation than tissue. A low transmit power was used to obtain a realistic signal-to-noise ratio. An illustration of the *in vitro* setup is shown in Fig. 4.4. A pump was used to control the stationary flow in the tube in the phantom. The liquid used to simulate blood is a mixture of Orgasol (polymers with similar size as red blood cells) and water [12]. The tube inner diameter was about 3 mm. In Tab. 4.1 the acquisition parameters used for the *in vitro* experiments can be found. From the parameters given in Tab. 4.1 the angle to the first grating lobe can be calculated from Eqn. (4.4) to be 57° . So for a transmit angle of 10° the first grating lobe will be at 47° .

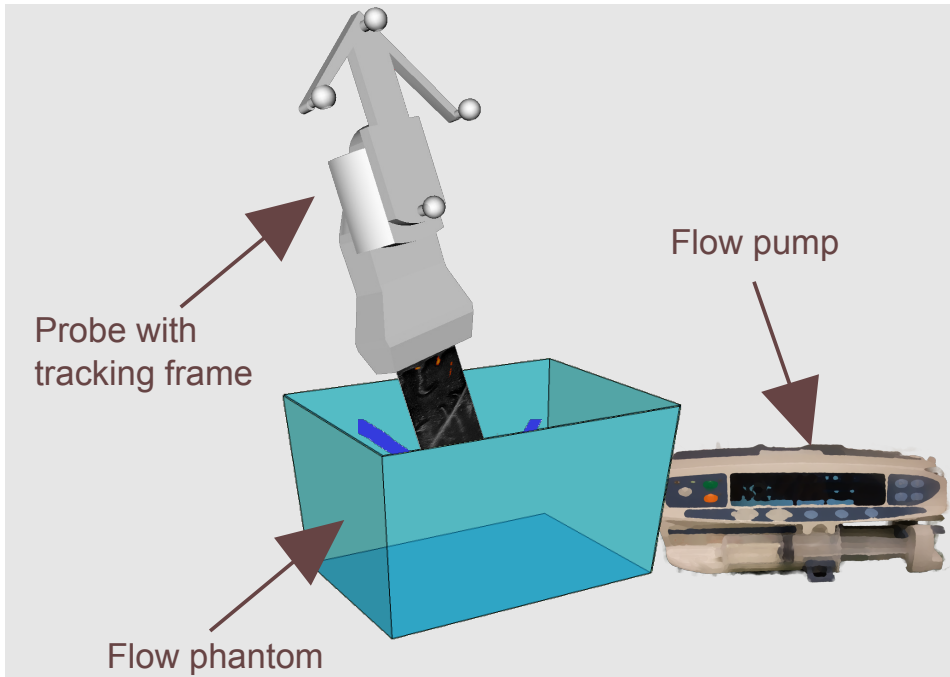


Figure 4.4: The *in vitro* setup used to validate the compounding approach, where stationary flow were generated using a pump.

4.2.5 In vivo recordings

For *in vivo* recordings the transmitted pressure field must satisfy the limits set by the US Food and Drug Administration (FDA). The custom real-time imaging setup used in the *in vitro* setup has at current time not been measured with regards to acoustic safety, so a clinical approved high end scanner was initially used for *in vivo* recordings. We then used a GE Vingmed E9 ultrasound scanner with a GE 11L linear array transducer (GE Vingmed Ultrasound, Horten, Norway). A direct link between the ultrasound scanner and the navigation computer provided the in-house navigation system with real-time ultrasound data as video-grabbed images. Real-time compounding of color flow images from different angles is not available on the scanner. Therefore three different acquisitions were done, with three different transmit angles. Afterwards the three data acquisitions were combined to one 3-D volume based on the same optical position information as previously described.

The method was tested on a blood vessel (radial artery) in the forearm of a healthy volunteer. The diameter of the blood vessel is about 3 mm. The arm was held in a fixed position during the ultrasound acquisitions with three different imaging angles.

We further evaluated the potential of the approach in the intraoperative context of neurovascular surgery, where both the presence of blood flow, and the flow

Table 4.1: In vitro acquisition parameters

Scanner	SonixMDP
Probe	L14-5
Pitch	0.3048 mm
Transmit frequency	6.0MHz
PRF	2.2kHz
Ensemble size	12
Interleave group size	8
Transmit and receive angles	-10°,0°,10°

direction and velocity are of interest. An arteriovenous malformation (AVM) is an abnormal connection between the arteries and veins in the brain, bypassing the capillary vessel network. AVMs can be treated by embolization in combination with microsurgery, where the larger abnormal feeding vessels (also called feeders) are clipped to reduce the flow in the AVM. In [13] it is shown that navigated ultrasound is useful for identification and clipping of feeders to AVMs. For the patient included in this study, the AVM was located close to the superior sagittal sinus vein. The ultrasound data were acquired after the bone flap had been temporarily removed from the skull, but before opening of the dura. The collection of data was approved by the local ethics committee and informed consent to participate in clinical research was given by the patient included in the study.

In Tab. 4.2 the acquisition parameters used for the *in vivo* trials can be found.

Table 4.2: In vivo acquisition parameters

	Radial artery	AVM
Scanner	Vivid E9	Vivid E9
Probe	11L	11L
Transmit frequency	7.1MHz	8.3MHz
PRF	0.75kHz	2.5kHz
Transmit and receive angles	-10°,0°,10°	-10°,0°,10°

4.3 Results

4.3.1 In vitro experiments

The algorithm for transmitting and processing multiple transmit angles was implemented on a research scanner to show the feasibility of the method. The results from the *in vitro* trials are shown in Fig. 4.5. There is a drop-out with the standard imaging setup with only one transmit angle, but by compounding data from different transmit angles no drop-outs is shown in the 3-D model in Fig. 4.5b.

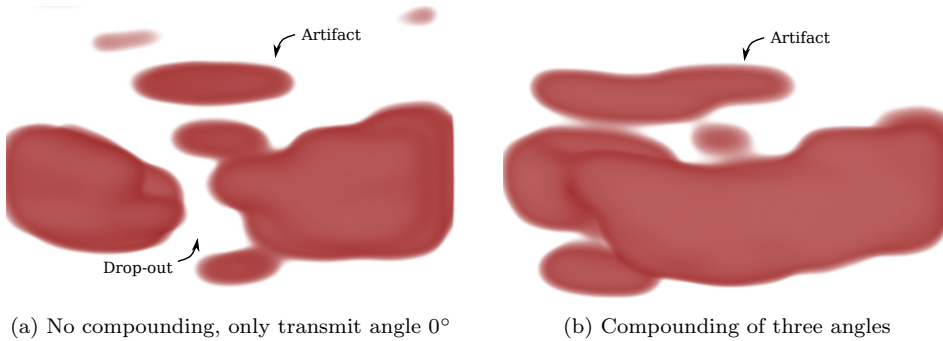


Figure 4.5: *In vitro* results showing the generated 3-D model with only one angle and compounding of three angles. The data are acquired on the research scanner with a custom scan sequence with three different transmit angles. A strong signal from tube can be seen as an artifact in the images.

4.3.2 In vivo feasibility

In Fig. 4.6 the generated 3-D volume of the radial artery in the forearm of a healthy volunteer is shown. In Fig. 4.6a-c the result from standard imaging with one angle is shown, and in Fig. 4.6d the result from compounding of three different angles is shown. The drop-outs are at different positions resulting in a compounded 3-D volume, Fig. 4.6d, with significantly less drop-outs. The *in vivo* data were acquired with acquisition parameters given in Tab. 4.2.

The 3-D volume of the AVM, shown in Fig. 4.7, had a very complex structure. This AVM had in total four main feeders, but only two of them were detected on the preoperative MR images. All four feeders were detected with ultrasound during the surgery and were successfully clipped. The red-colored volume is the result without compounding, and the green-colored volume shows the extra information obtained by compounding of three different transmit angles. As can be observed, compounding significantly improves the final 3-D volume. At point I in Fig. 4.7 one of the smaller feeding vessels is in fact only visible after compounding of the different transmit angles. The data were acquired with acquisition parameters given in Tab. 4.2.

4.4 Discussion

In this work we have shown how compounding of color flow images with different steering angles can be used in combination with a position system to improve 3-D images of vascular flow. The 3-D image can be useful for better visualization of the complex architecture structure of blood vessels.

Velocities below v_{\min} given in Eqn. (4.2) will be filtered out by the clutter filter. The clutter filter is necessary to filter out the signal from the tissue, and will also remove the lower velocities in the blood. Low velocities in the beam direction will

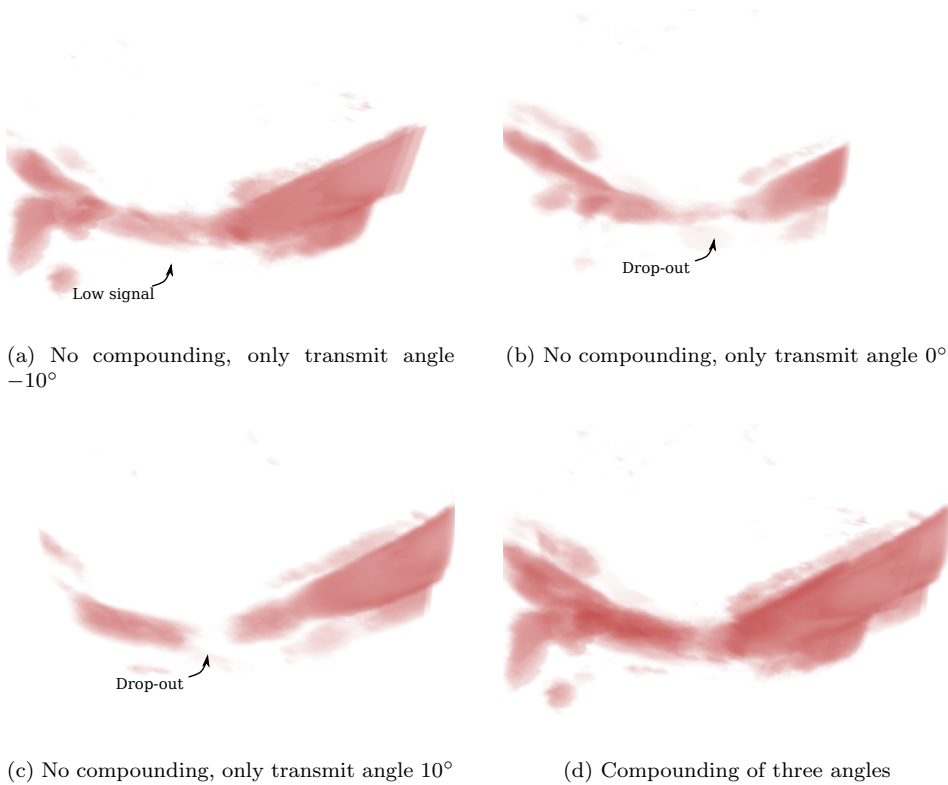


Figure 4.6: *In vivo* results showing the generated 3-D model of the radial artery of a healthy volunteer. The diameter is about 3mm

then lead to a drop-out in the 3-D model, so multi-angle imaging will for some angle increase the axial velocity and then also reduce the drop-outs.

Compounding images from different imaging angles for flow imaging is currently not available on commercial scanners. But compounding of tissue images from different imaging angles is commonly used to reduce speckle noise and anisotropy in high-end ultrasound systems, improving image contrast and appearance [14]. We have implemented compounding of flow images on a research scanner and the *in vitro* trails shows the feasibility of the method.

The custom made scan sequence must be clinical approved before testing on patients is allowed. To demonstrate the feasibility of compounded color flow for 3-D flow imaging on *in vivo* data a clinical approved scanner was therefore initially used. Data from three different transmit angles were acquired by three acquisitions. This approach also requires a very accurate and well calibrated position system. Small errors in the calibration will lead to spatial mismatch between the different acquisitions, and smearing of the final volume. A real-time implementation for compounding of the flow images will simplify the acquisition and is less influenced

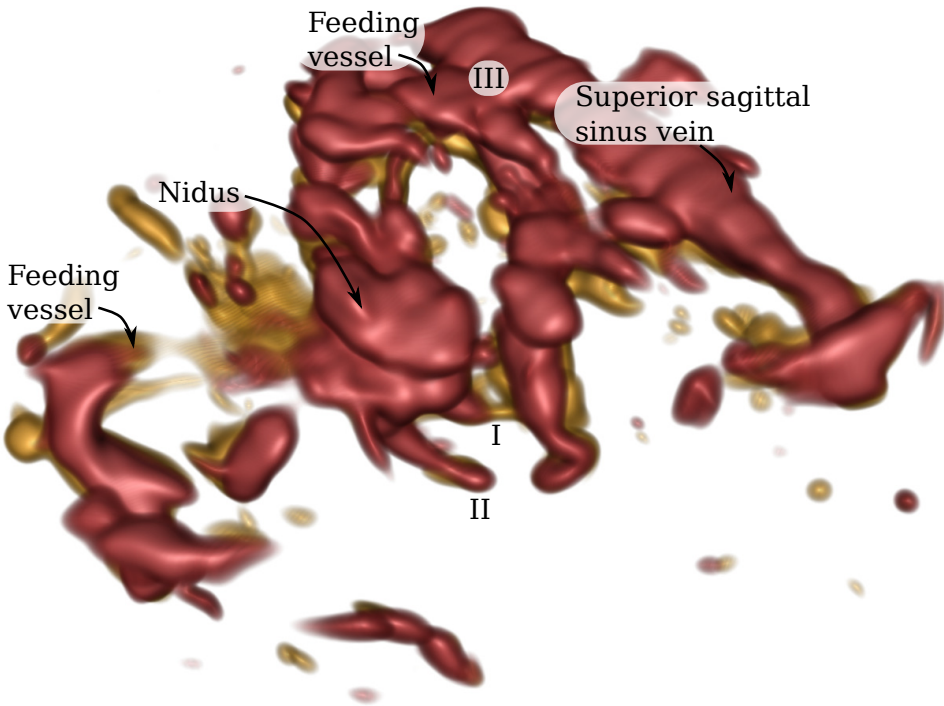


Figure 4.7: *In vivo* results showing the generated 3-D model of an intracranial arteriovenous malformation with compounding of three different transmit angles. The red-colored data are the result without compounding, and the yellow-colored data shows the extra data obtained by compounding of three different transmit angles.

by small calibration errors.

The *in vivo* trials, in Fig. 4.7, from neuro surgery shows that the method has potential to improve the 3-D image quality of blood vessels in a clinical setting. The method can easily be adopted to the clinical practice for neurosurgery, where a position system may already be in use. Compounding of multiple angle transmissions will improve the 3-D image quality by reducing the drop-outs, and lead to easier understanding of complex vessel structures.

The method presented here will limit drop-outs in vessels crossing the scan direction, as seen in the *in vitro* and *in vivo* trials in Fig. 4.5-4.7. Blood vessels going out of the 2-D plane will however not be covered in the freehand acquisition scheme, and drop-outs will therefore still occur for some blood vessels. The drop-out II in Fig. 4.7 was identified as a blood vessel going out of the 2-D plane. By doing two acquisitions in orthogonal directions the number of drop-outs will be reduced even more.

As a new compounded image can be generated as each new frame is acquired, there should be no reduction in the frame rate for image compounding. For B-mode imaging on commercial scanners approximately the same frame rate is obtained

for compounding as for standard imaging, so it should also be feasible to obtain approximately the same total frame rate for compounding of flow images as for standard flow imaging. A frame rate of about five frames per second were obtained on the research scanner when a region of interest covered half the probe width. On most high-end scanners multi line acquisition is possible and will increase the frame rate. So a frame rate of approximately ten frames per second with a full sector should be possible on a high-end scanner.

Another benefit of using multiple angle transmission is that a wider 2-D image sector can be obtained, by also including the data where no compounding information exists. This can lead to a 3-D model covering more of the complex vessel structure. In intraoperative settings a larger field of view can often be useful to cover all the vessels of interest. Some parts of the image will however lack the benefits of multiple angle transmissions.

When imaging a vessel structure with high range of velocities more of the lower velocities will be in the stop band of the clutter filter, and more drop-outs will occur. A larger transmit angle can be necessary to eliminate the drop-outs from vessels with very low velocities. As given in Eqn. (4.4) this will result in more influence from grating lobes for a given probe, so a compromise must be done. Larger transmit angles will also reduce overlapping area, hence reduce the area benefitting from advantages of compounded flow information.

Flashing artifacts in the image can occur during freehand scan due to abrupt movement of the ultrasound probe, or due to tissue movement caused by pulsatile pressure. A flash will appear as a blob in the 3-D scene, and complicate the interpretation of the vessel structure. By increasing the stop band of the clutter filter more flash artifacts will be filtered out. However, also more of the blood velocities will be filtered out. This will lead to more drop-outs in 2-D, but compounding of different imaging angles may still reduce the drop-outs in the final images. This approach will not work for unwanted movement in the same direction as the blood flow, and the effect remains to be evaluated.

Further work will investigate how an acquisition based on parallel receive beamforming can be used to improve the method. By transmitting an unfocused and wide ultrasound beam, a larger region can be covered by one transmission, and multiple image lines can be generated in parallel. This will result in a higher frame rate than in conventional flow imaging, and allows for compounding of more angles for improved contrast and improved detection of blood vessels with low axial velocity. Parallel receive beamforming, its benefits and limitations, are further described in [15, 16]. The extra information from transmitting multiple angles can also be combined to provide vector velocity information, also known as vector Doppler. More detailed flow information can be useful to understand flow pattern in complex vascular structures. The technique requires a short time period between the different angles to ensure similar flow conditions. For conventional focused imaging the frame rate is too low so the time between each angle will be too long.

Even with all the drop-outs in the 3-D image of the AVM in Fig. 4.7 eliminated there will still be improvements in the image quality that should be done. Due to an inadequate spatial resolution the vessels are smeared out, and for instance at

point III in Fig. 4.7 it is not correct that one of the feeding vessel of the AVM is connected to the superior sagittal sinus vein. There are also some smaller vessels not interesting for the AVM surgery that can complicate the interpretation of the 3-D image. Further work should study how to improve these issues.

Although indications are given for the usefulness of compounding of flow images from multiple transmit angles in the neurosurgical context, a patient study is needed to properly establish the clinical value of the method.

4.5 Conclusion

Improved 3-D volumes of blood vessels were obtained by using free-hand 3-D ultrasound imaging with compounding of multiple transmit angles and position sensor information. *In vitro* and *in vivo* experiments revealed an improvement of 3-D images by eliminating drop-outs in the blood vessel structure. However, imaging of blood vessels crossing perpendicular out of the 2-D scan plane will still lead to a drop-out. This can be solved by introducing an extra acquisition, done in a perpendicular scan direction. Potential clinical use was demonstrated for vascular blood vessels and neurosurgical applications.

REFERENCES

- [1] G. Unsgaard, O. M. Rygh, T. Selbekk, T. B. Müller, F. Kolstad, F. Lindseth, and T. N. Hernes, “Intra-operative 3D ultrasound in neurosurgery,” *Acta neurochirurgica*, vol. 148, no. 3, pp. 235–253, Mar. 2006. [Online]. Available: <http://www.ncbi.nlm.nih.gov/pubmed/16362178>
- [2] B. B. Goldberg, J. B. Liu, and F. Forsberg, “Ultrasound contrast agents: a review.” *Ultrasound in medicine & biology*, vol. 20, no. 4, pp. 319–33, Jan. 1994. [Online]. Available: <http://www.ncbi.nlm.nih.gov/pubmed/22161614>
- [3] B. Dunmire, K. W. Beach, K. H. Labs, M. Plett, and D. E. Strandness Jr, “Cross-beam vector Doppler ultrasound for angle-independent velocity measurements,” *Ultrasound in medicine & biology*, vol. 26, no. 8, pp. 1213–1235, 2000.
- [4] S. Bjærum, H. Torp, T. r. Bakke, and K. Kristoffersen, “Automatic Selection of the Clutter Filter Cut-off Frequency in Ultrasound Color Flow Imaging,” *Ultrasonics, Ferroelectrics and Frequency Control, IEEE Transactions on*, vol. 49, no. 2, pp. 204–216, 2002.
- [5] T. L. Szabo, *Diagnostic ultrasound imaging: inside out*. Academic Press, 2004.
- [6] C. Askeland, F. Lindseth, O. V. Solberg, J. Beate, L. Bakeng, and G. A. Tangen, “CustusX : A Research Application for Image-Guided Therapy,” *Insight Journal*, pp. 1–8, 2011.
- [7] F. Lindseth, T. Langø, J. Bang, and T. N. Hernes, “Accuracy evaluation of a 3D ultrasound-based neuronavigation system.” *Computer aided surgery : official journal of the International Society for Computer Aided Surgery*, vol. 7, no. 4, pp. 197–222, Jan. 2002. [Online]. Available: <http://www.ncbi.nlm.nih.gov/pubmed/12454892>
- [8] R. H. Chesarek, “Ultrasound imaging system for relatively low-velocity blood flow at relatively high frame rates,” 1989.
- [9] H. Torp, “Clutter rejection filters in color flow imaging: a theoretical approach.” *IEEE transactions on ultrasonics, ferroelectrics, and frequency*

-
- control*, vol. 44, no. 2, pp. 417–24, Jan. 1997. [Online]. Available: <http://www.ncbi.nlm.nih.gov/pubmed/18244139>
- [10] C. Kasai, K. Namekawa, A. Koyano, and R. Omoto, “Real-time two-dimensional blood flow imaging using an autocorrelation technique,” *IEEE Trans. Sonics Ultrason*, vol. 32, no. 3, pp. 458–464, 1985. [Online]. Available: http://server.elektro.dtu.dk/personal/jaj/31545/documents/kasai_et_al.1985.pdf
- [11] O. V. Solberg, F. Lindseth, H. Torp, R. E. Blake, and T. a. Nagelhus Hernes, “Freehand 3D ultrasound reconstruction algorithms—a review.” *Ultrasound in medicine & biology*, vol. 33, no. 7, pp. 991–1009, Jul. 2007. [Online]. Available: <http://www.ncbi.nlm.nih.gov/pubmed/17512655>
- [12] K. Ramnarine and D. Nassiri, “Validation of a new blood-mimicking fluid for use in Doppler flow test objects,” *Ultrasound in medicine & ...*, vol. 24, no. 3, pp. 451–459, 1998. [Online]. Available: <http://www.sciencedirect.com/science/article/pii/S0301562997002779>
- [13] G. Unsgaard, S. Ommedal, O. M. Rygh, and F. Lindseth, “Operation of Arteriovenous Malformations Assisted by Stereoscopic Navigation-controlled Display of Preoperative Magnetic Resonance Angiography and Intraoperative Ultrasound Angiography,” *Neurosurgery*, vol. 56, no. Supplement 2, pp. 281–290, Apr. 2005.
- [14] S. Huber, M. Wagner, M. Medl, and H. Czembirek, “Real-time spatial compound imaging in breast ultrasound,” *Ultrasound in medicine & biology*, vol. 28, no. 2, pp. 155–163, 2002.
- [15] D. P. Shattuck, M. D. Weinshenker, S. W. Smith, and O. T. von Ramm, “Explososcan: a parallel processing technique for high speed ultrasound imaging with linear phased arrays.” *The Journal of the Acoustical Society of America*, vol. 75, no. 4, pp. 1273–82, Apr. 1984. [Online]. Available: <http://www.ncbi.nlm.nih.gov/pubmed/6725779>
- [16] T. Hergum, T. Bjåstad, K. Kristoffersen, and H. Torp, “Parallel beamforming using synthetic transmit beams.” *IEEE transactions on ultrasonics, ferroelectrics, and frequency control*, vol. 54, no. 2, pp. 271–80, Feb. 2007. [Online]. Available: <http://www.ncbi.nlm.nih.gov/pubmed/21384334>

Chapter 5

Fast 3-D reconstruction of the carotid artery bifurcation based on real-time 2-D segmentation

Daniel Høyer Iversen¹, Sigurd Storve¹, Torbjørn Dahl², Hans Torp¹ and Lasse Lovstakken¹

¹MI Lab and Dept. of Circulation and Medical Imaging, Norwegian University of Science and Technology, Trondheim, Norway

² St Olavs Hospital, Trondheim, Norway

Abstract — In identification and diagnosing of plaque in the carotid artery, 3-D visualization showing the geometry and extent of the plaque may be clinically useful. However, due to current non-availability of 3-D vascular ultrasound probes this is currently not possible. In this work we aim to generate on-the-fly 3-D models of the carotid artery from automatic segmented 2-D ultrasound images based on a Kalman filter approach. During acquisition the position and orientation of each cross-sectional image of the carotid were registered by an accurate position sensor system, and further combined to reconstruct a 3-D model of the carotid artery lumen. The parameters in the automatic segmentation algorithm were tuned on a training set consisting of data from five people. The method was evaluated on a straight tube in vitro phantom and compared with a ground truth, resulting in an error of 0.14 mm measured by the modified Hausdorff distance. The parameters in the automatic segmentation algorithm were tuned

on a test set consisting of data from five people. A manual segmentation done by two experts evaluators, resulting in an inter-observer error similar to the error of the manual segmentation compared with the automatic segmentation. The fast and relatively accurate reconstruction of 3-D carotid models may be suited to bedside 3-D visualization and volume estimation of moderate to large plaques.

5.1 Introduction

Stroke is currently the second leading cause of death worldwide [1], with a prevalence that is expected to increase in the coming years due to the aging population and lifestyles associated with obesity. Plaque in the carotid artery is responsible for approximately 20% of all strokes of thromboembolic origin [2], and plaques in the carotid are indicative of systemic development of atherosclerosis. Hence, there is a need for improved diagnostic methods to detect and understand the progression of diseases in the carotid artery. Current noninvasive methods for evaluation of plaques in the carotid artery include magnetic resonance (MR) [3] and ultrasound. MR is more expensive, time consuming, and demanding logistically, than ultrasound, but may provide 3-D imaging in this context. Due to portability and the easy access to carotid imaging, ultrasound is currently the main modality for identifying and grading carotid plaques. Due to the three-dimensional (3-D) extent of the plaque, 3-D imaging is desired in order to provide information about the distribution, volume, and degree of plaque protruding the carotid lumen. However, an ultrasound probe capable of real-time 3-D imaging of the carotid artery is not currently available. This modality thus only provides a limited ability to visualize how the plaque is distributed in 3-D.

Previous work has described a method to reconstruct 3-D B-mode images based on freehand scanning with magnetically tracking of the carotid artery for registration with MR images [4]. In [5] a custom mechanical linear 3-D US scanning system was used to generate a 3-D volume of the carotid artery. The 3-D volume was further used for manual registration of plaque volume. In [6] a 3-D volume of the carotid artery, generated from 2-D slices from a probe attached to a motorized mover, was shown to provide potentially useful information about changes in carotid plaque volume.

A 3-D model of the carotid artery can be generated from segmented 2-D B-mode frames registered in space using a position sensor system. Manual segmentation of 2-D ultrasound images has proven useful for quantification of plaque in the carotid artery [7]. The 2-D images were further reconstructed to a 3-D volume by using the segmented surface. Previous work have studied segmentation of 2-D images of the carotid artery by a deformable model as presented in [8]. Such a deformable model can with benefit be fitted to the data in a Kalman filter framework, as have been shown for segmentation of ultrasound images from echocardiography [9–12].

In this work we aim to generate 3-D volumes of the carotid artery by acquiring 2-D B-mode data with position and orientation of each scan plane. The position

and orientation of the probe is registered by an optical sensor. The 2-D images are segmented on-the-fly by a Kalman filter approach, where edge detection and block matching are used as input measurements [13]. We have chosen to use a deformable model to ensure a continuous boundary and include prior information of the vessel shape. The method has the advantage of being fast, almost automatic and gives reliable 3-D models.

Fast 3-D reconstruction of the carotid artery and associated plaques during patient examination may be beneficial when evaluating the plaque degree and extents, important for instance for deciding whether the patient should undergo a surgical carotid endarterectomy procedure.

This paper has been organized as follows. In Section II, the experimental setup is presented, as well as the method to segment ultrasound data and reconstruct the data to a 3-D volume. In Section III, tuning of the segmentation algorithm and *in vitro* results are presented. A validation of the method is done by comparing the automatic segmentation with manual segmentation from experts. These results and potential future work are discussed in Section IV. In Section V conclusions are presented.

5.2 Methods

5.2.1 Experimental setup and data acquisition

The setup used in the laboratory and for the patient-study is shown in Fig. 5.1 and Fig. 5.2. The system consists of a computer for image processing and navigation, running the in-house software called CustusX [14] (SINTEF Medical technology, Health Research, Trondheim, Norway), connected to an optical 3-D position tracker (NDI Polaris Spectra; Northern Digital, Waterloo, Canada). The accuracy (RMS error) of the position tracker is reported by the manufacturer to be 0.25 mm, however, due to calibration uncertainties the average error of the system has been measured to be 1.4 mm [15]. This calibration error is not a stochastic error, but mainly a constant spatial offset. To acquire ultrasound images, we used a GE Vingmed E9 ultrasound scanner with a GE 11L linear array transducer (GE Vingmed Ultrasound, Horten, Norway). A direct link between the ultrasound scanner and the navigation computer provided the in-house navigation system with real-time ultrasound data, as seen in Fig. 5.2. 2-D ultrasound images were obtained by free-hand, cross-sectional scanning along the carotid vessel, where the position and orientation of the plane were stored during acquisition.

5.2.2 On-the-fly image segmentation framework

For segmentation of the tissue (B-mode) images we used a segmentation library called Real-time Contour Tracking Library (RCTL) presented in [13], where global transformation parameters (translation, scaling, and rotation) and local transformation parameters are defined in a state vector, \mathbf{x}_k and updated in a Kalman filter framework. The local transformation includes the deformation of the initial model.

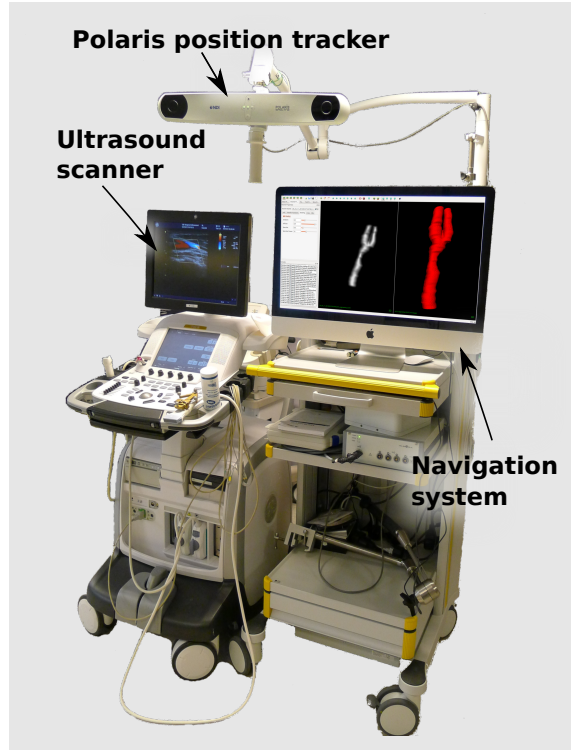


Figure 5.1: The navigation system. Showing the position tracker, the ultrasound scanner and the navigation system. (CustusX)

This framework was initially developed for real-time 3-D segmentation of cardiac chambers, and was in this work adapted for 2D cross-sectional carotid imaging and segmentation.

The inputs to the Kalman filter are the initial model, edge detection results, block matching results and the state vector, \mathbf{x}_{k-1} , from the previous time step. An extended Kalman filter with a Jacobian matrix was used, since the measurement model is a non-linear function of the state vector. The filter consists of a prediction step and an update step:

The prediction step. A regularization parameter defines the deformability of the model from an initial model. In this study we have chosen a circular shape as the initial model, since we are acquiring cross-section images of blood vessels. The prediction step is a matrix multiplication which has a regularization effect on the model, i.e. it pulls the state vector towards an initial state \mathbf{x}_0 :

$$\bar{\mathbf{x}}_k = \mathbf{x}_0 + \mathbf{A}(\hat{\mathbf{x}}_{k-1} - \mathbf{x}_0) \quad (5.1)$$

where A is a matrix of regularizing parameters weighting measured values towards model accuracy.

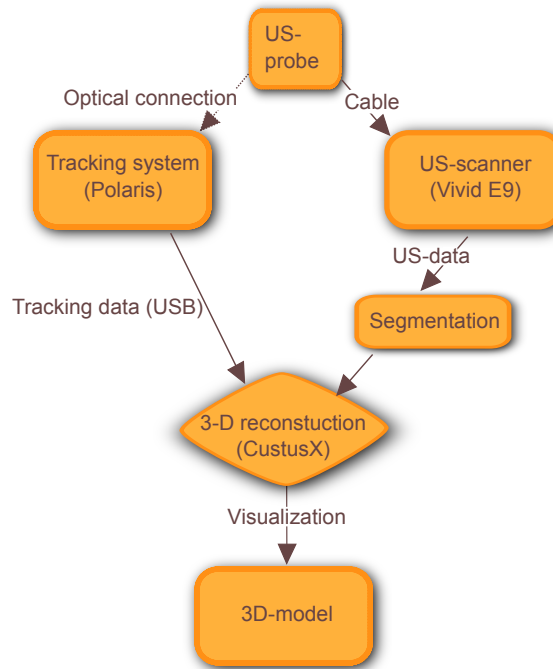


Figure 5.2: Block diagram of the main connections between the systems used.

The update step. The results from edge detection and block matching are the input to the update step. The edge detection is computed at predefined points on the curve defining the model in the previous frame. At each of these points a search profile of image samples are extracted in the direction perpendicular to the curve, as illustrated in Fig. 5.3a. The estimated edge results in a displacement vector with length $v_{k,j}$ at each point j . We evaluated four different edge detections criteria for finding the inner edge of the carotid lumen:

- 1) **Gradient** - Estimates the edge at the position of the maximum gradient in a smoothed version of the image samples.
- 2) **Max** - Estimates the edge at the position of the maximum intensity in a smoothed version of the image samples.
- 3) **Peak** - Estimates the edge at the position where the intensity level changes from one intensity level, to another level, and then back again.
- 4) **Step** - Estimates the edge at the position where the intensity level changes from one intensity level to another level.

The block matching algorithm searches for a matching 2-D kernel (template) extracted at predefined points on the curve in the previous frame. The sum of

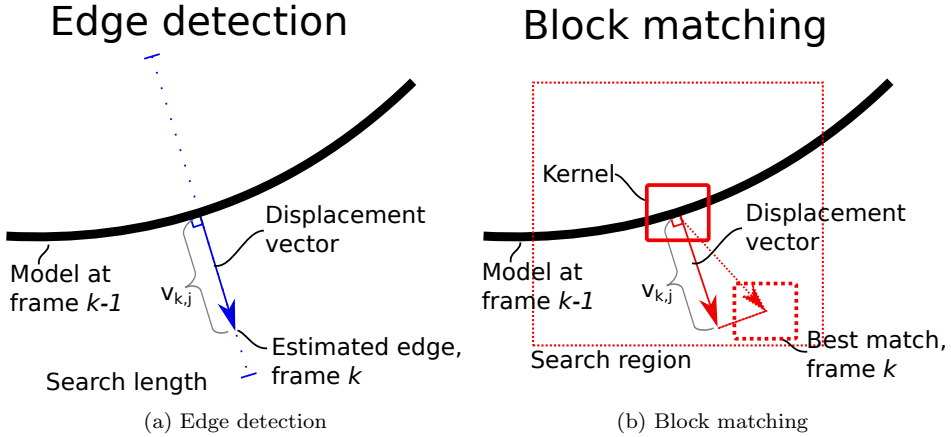


Figure 5.3: Illustration of how the displacement vector from edge detection and block matching is calculated.

absolute differences was used as matching criteria to find the local movement from the previous frame. The Lucas-Kanade optical flow algorithm [16] was used to estimate sub-sample displacements. The estimated movement from the block matching is illustrated in Fig. 5.3b with a dotted line. The final displacement vector was chosen as the projection perpendicular to the model surface with length $v_{k,j}$, as shown in Fig. 5.3b.

Simple outlier rejection was performed for both edge detection and block matching by excluding an estimation if it differs too much from the four neighboring displacement vectors.

The updated state estimate \mathbf{x}_k for frame k is given as

$$\hat{\mathbf{x}}_k = \bar{\mathbf{x}}_k + \mathbf{K}_k \mathbf{v}_k, \quad (5.2)$$

where \mathbf{K}_k is the Kalman gain matrix and \mathbf{v}_k consists of the length of all the displacement vectors, $v_{k,j}$ from the block matching and the edge detection. A noise parameter, σ , for each measurement is included in \mathbf{K}_k to prioritize the edge detection or block matching.

The Kalman filter procedure can be repeated N times for the same data to iteratively improve on the segmentation results. For more details on the segmentation method we refer to [11, 17].

5.2.3 Segmentation setup

For initializing the algorithm, two seed points were manually defined in one 2-D image to identify the internal and the external carotid artery. To find best edge detection criteria the four different edge detection criteria were tested, by only applying the edge detection part of the algorithm on the data in the training set. The regularization parameter was tuned to make a deformable model that could

adapt to changes inferred by plaques, but not too influenced by noise in the image. The weights between the different inputs were tuned to optimize the segmentation algorithm.

The estimation was repeated 15 times for each frame to iteratively find the best segmentation.

To further improve the segmentation results the Kalman filter is used both forward and backwards, i.e after finishing the forward step the Kalman filter is applied on the frames in the opposite order, starting from the common carotid artery. To ensure a consistent behavior the models are restricted to not differ more than a given distance. The state estimate from the forward step, $\hat{\mathbf{x}}_{F,k}$ and the backward step $\hat{\mathbf{x}}_{B,k}$ is combined as the simple average.

5.2.4 3-D reconstruction

After real-time segmentation the segmented 2-D frames were smoothed by averaging over a number of frames. The 2-D frames were further reconstructed to a 3-D vessel model based on the position information. The 3-D reconstruction was done by a Pixel Nearest Neighbor algorithm as described in [18]. Each pixel in all the 2-D frames is filled in the nearest voxel in the 3-D volume. The reconstructed 3-D volume is finally Gaussian smoothed.

5.2.5 Data material

To validate the 2-D segmentation of the model an *in vitro* setup was used consisting of a straight tube with an inner diameter of 6 mm. The tube is immersed in a material with similar properties as tissue, and a pump controlled a stationary flow of a blood mimicking fluid.

In vivo data was acquired from three healthy volunteers and nine patients with suspected arterial plaque from the outpatient vascular clinic. The image acquisition was done following the regular patient examination. A complete ultrasound recording covering the common, external and internal carotid arteries was done by slowly sliding the ultrasound probe from the neck towards the head, which took approximately 20 seconds. The study was approved by the national ethics committee and written consent was obtained from all participants. The data from three healthy volunteers and two patients were used as training data to optimize the parameters in the segmentation algorithm. The data from five further patients were used for validation, while two patients were excluded due to severely noisy images.

5.2.6 Validation of the segmentation algorithm

To validate the segmentation algorithm, the automatic segmentations were compared with manual expert segmentation for *in vivo* data and a ground truth for the *in vitro* data. The Hausdorff distance was used as suggested to be a standard metric for comparing two different segmentations [19]. Let the two curves be represented as sets of points $\mathcal{A} = \{a_1, a_2, \dots, a_m\}$ and $\mathcal{B} = \{b_1, b_2, \dots, b_n\}$, then the



(a) Step one. Control nodes for a continuous curve were set to identify the vessel border



(b) Step two. Fine tuning of the manual segmentation.

Figure 5.4: Manual segmentation tool

Hausdorff distance is defined in [20] as

$$H(\mathcal{A}, \mathcal{B}) = \max(h(\mathcal{A}, \mathcal{B}), h(\mathcal{B}, \mathcal{A})) \quad (5.3)$$

where

$$h(\mathcal{A}, \mathcal{B}) = \max_{a \in \mathcal{A}} \min_{b \in \mathcal{B}} \|a - b\| \quad (5.4)$$

and $\|\cdot\|$ here is chosen to be the Euclidean norm. The Hausdorff distance is the greatest disagreement between curve \mathcal{A} and \mathcal{B} , so only one mismatched point is enough to make the Hausdorff distance high between curve \mathcal{A} and \mathcal{B} . In [21] a modified Hausdorff distance is given as:

$$h(\mathcal{A}, \mathcal{B}) = \frac{1}{N_{\mathcal{A}}} \sum_{a \in \mathcal{A}} \min_{b \in \mathcal{B}} \|a - b\|. \quad (5.5)$$

The modified Hausdorff distance consider the mismatch from all points in the curve. Both the Hausdorff distance and the modified Hausdorff distance are presented in the results.

To validate the manual segmented *in vitro* data, a ground truth is constructed as a straight tube with 6 mm diameter and spatially oriented by matching the centerlines from the generated ground truth and the automatic segmented model with CustusX. The 3-D meshes were compared by the Hausdorff distance and the modified Hausdorff distance.

To validate the automatic segmented *in vivo* data, manual segmentation was done by expert evaluators for five patients. The segmentation algorithm was tested without any further modifications. An in-house software was developed for manual segmentation of ultrasound images. Control nodes for a continuous curve were set to identify the vessel border, as seen in Fig. 5.4a. Afterwards could the curve be modified to fine tune the manual segmentation, as seen in Fig. 5.4b. Manual segmentation was made by a vascular surgeon and a cardiologist, both with extensive

knowledge of carotid artery imaging. They manually segmented 15 frames from each patient. The frames were chosen with the bifurcation approximately as the middle frame, and the rest of the frames equally spread over the carotid artery.

5.3 Results

5.3.1 Optimization of the segmentation parameters

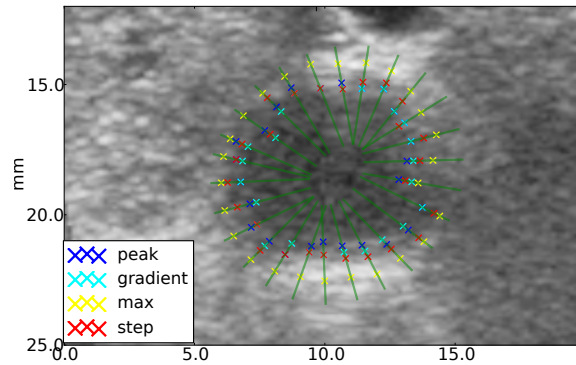


Figure 5.5: The different edge detection algorithms tested on a cross-section B-mode image of the common carotid artery. The green lines illustrate the search length for the edges, and the X marks the detected edge with the different edge detectors. Only every third edge detector is visualized.

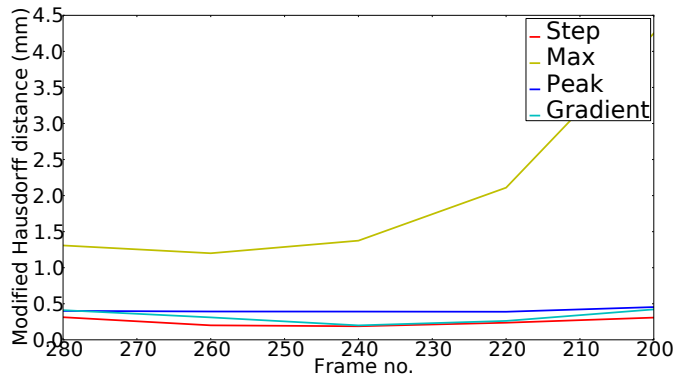


Figure 5.6: The different edge detector algorithms tested on serial B-mode images and validated against manual segmentation

The *in vivo* results from the different edge detection algorithms are shown in Fig. 5.5. The green lines illustrate the search length for the edges, and the X marks

the detected edges by the different edge detectors (only every third edge detection is visualized). The max criteria is in most cases estimating the edges too far from the center, while the peak and gradient criteria in most cases estimating the edges too close to the center. In Fig. 5.6 the automatic segmentation is compared with a manual segmentation for the different edge detector types. The step-criteria proved the best overall choice for the current data material.

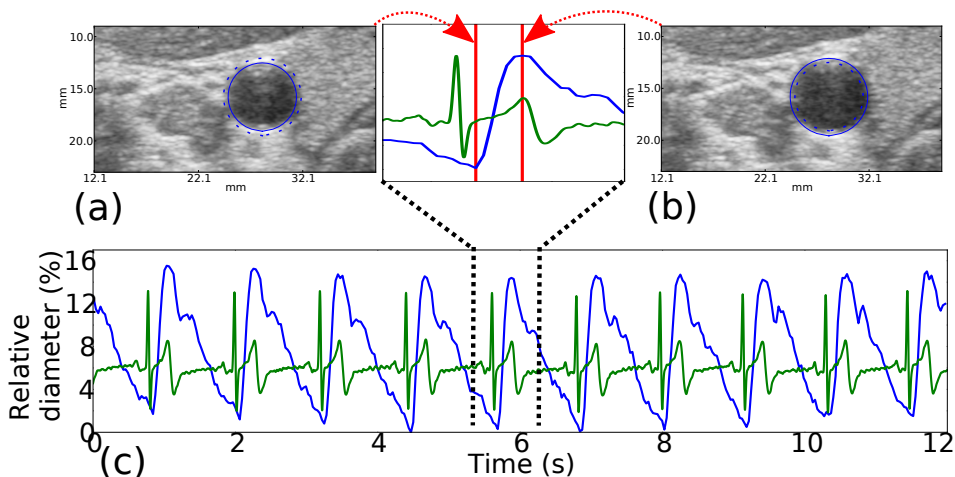


Figure 5.7: (a) B-mode image where the blue solid line shows the automatic segmentation of 2-D frames of the common carotid artery of a healthy volunteer at the smallest diameter. The dotted line shows the largest diameter.

(b) B-mode image where the blue solid line shows the automatic segmentation of 2-D frames of the common carotid artery of a healthy volunteer at the largest diameter. The dotted line shows the smallest diameter.

(c) The blue line shows the diameter estimated from the automatic segmented as a function of the time. The green line is the scaled ecg signal as a function of time. The red lines mark the position of the two 2-D frames.

The search lengths used for the edge detection and block matching are given in Tab. 5.1. The kernel size for block matching was chosen as 1.4 times the spatial resolution. A displacement vector was defined as an outlier if it differed more than 1 mm from the neighbors. The search length is larger than the physiological movement expected. In noisy images, such as in Fig. 5.11a, the method may partly fail to segment the blood vessel, but due to a long search length the method is able to relocate the edge in a later frame.

The regularization parameters were tuned to make a deformable model that could capture vessel wall variation inferred by plaque and pulsation, while smoothing to be more robust in noisy data. The ultrasound data for one carotid artery were acquired during about 20-30 heart cycles, so the pulsation will influence the final 3-D model. To test how consistently the segmentation method is a data set

Table 5.1: Parameters for edge detection and block matching

Edge detection

Search length	3.75 mm
Noise parameter, σ	0.50 mm

Block matching

Search length	1.00 mm
Kernel size	0.40 mm, 0.30 mm
Noise parameter, σ	0.90 mm

were acquired with the probe held in a constant position during several heart cycles at the common carotid artery of a healthy volunteer. The estimated relative diameter and the electrocardiography (ecg) signal is plotted as a function of time in Fig. 5.7. The figure also shows how the segmentation method captures both the smallest diameter (Fig. 5.7a) and the largest diameter (Fig. 5.7b).

5.3.2 Validation of the segmentation algorithm

To validate the 3-D segmentation of the model an *in vitro* setup with a 3-D ground truth was compared. The Hausdorff distance and the modified Hausdorff distances were calculated as given in Eqn. (5.4) and Eqn. (5.5) resulting in an error given in Tab. 5.2.

Table 5.2: Comparison with automatic segmentation and a ground truth in 3-D

Hausdorff distance	Modified Hausdorff distance
0.55 mm	0.14 mm

The automatic segmentation of five patients were compared with manual segmentation. In Fig. 5.8 an example of manual and automatic segmentation is compared for three different positions. In Fig. 5.8a segmentation at the bifurcation is shown. The automatic segmentation has succeeded in merging the two models from the externa and interna carotid artery, and corresponds well with the manual segmentation from both of the experts. Fig. 5.8b and Fig. 5.8c show examples of segmentation of the interna and externa carotid artery. In Fig. 5.8b the red line, representing the manual segmentation of one of the experts, differs from the automatic segmentation. The other expert segmentation, represented with a green line, is however closer to the automatic segmentation. The median of results from the manual segmentation are presented in Tab. 5.3 and Fig. 5.9. Errors above 3 mm were considered as outliers and not included.

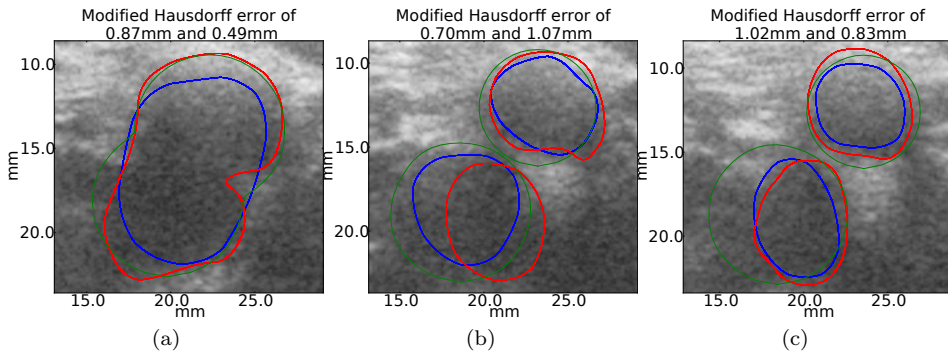


Figure 5.8: Manual segmentation and automatic segmentation of the same frames. Red and blue lines are manual segmentation and green lines are the automatic segmentation.

Table 5.3: The median error of the manual segmentations and the automatic segmentation

Metric	Auto ~ Expert 1+2	Auto ~ Expert 1	Auto ~ Expert 2	Expert 1 ~ Expert 2
Hausdorff	1.74 mm	1.72 mm	1.74 mm	1.69 mm
Mod. Hausdorff	0.84 mm	0.64 mm	0.96 mm	0.84 mm

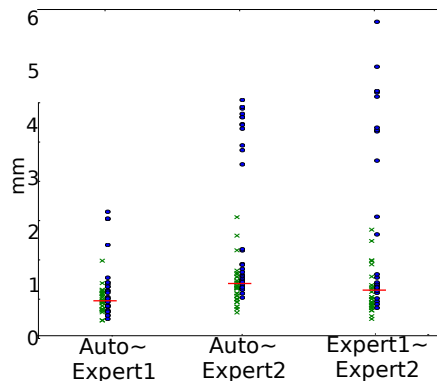
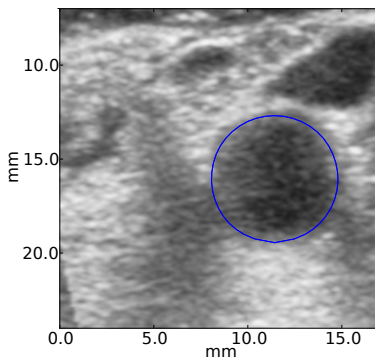


Figure 5.9: The modified Hausdorff errors of the comparison between the manual segmentations and the automatic segmentation for all the frames. The green x's show the errors for the common carotid artery, and the blue o's show errors after the bifurcation. The red horizontal line shows the median error.

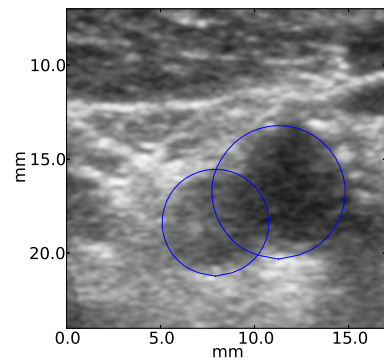
5.3.3 In vivo examples

The automatic segmentation of different parts of the carotid artery from a patient with plaque is shown in Fig. 5.10. The example is from the training set.

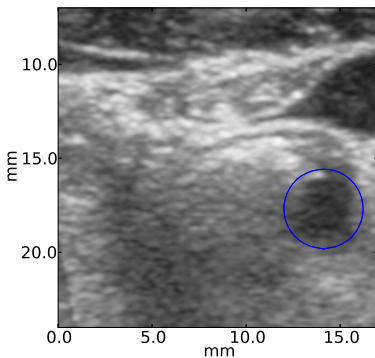
Examples of automatic segmentation is shown for the internal and external (Fig. 5.10a) carotid, and the carotid bifurcation (Fig. 5.10b). This illustrates how the two models merge together at the bifurcation, and how the union of the two models is used to generate the 3-D model. In Fig. 5.10c an example is shown where plaque in the left side of the vessel is correctly segmented, and in Fig. 5.10d an example with the common carotid artery correctly segmented is shown.



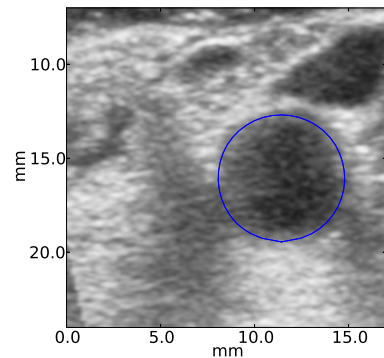
(a) Frame no 29. Internal and external carotid artery with automatic segmentation.



(b) Frame no 297. At the bifurcation of the carotid artery.



(c) Frame no 435. Common carotid artery with large plaque.



(d) Frame no 564. Common carotid artery.

Figure 5.10: 2-D images of carotid artery from a patient with plaque. The blue solid lines are automatic segmentation of the carotid artery.

Two of the most challenging frames are shown in Fig. 5.11. In Fig. 5.11a a small plaque in the upper part of the blood vessel is shown. Due to weak edges and regularization the model fails to segment the plaque. We believe that the dotted

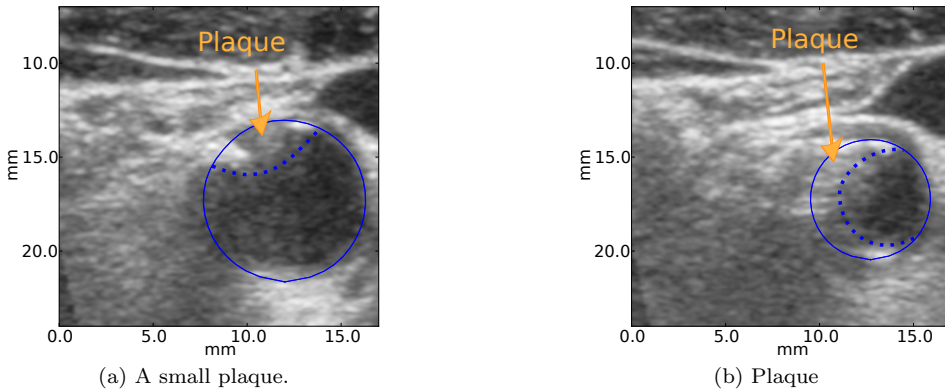


Figure 5.11: 2-D images of carotid artery from a patient with plaque. The blue solid lines are automatic segmentation of the carotid artery. The dashed lines are suggested manually corrections.

line indicates a more correct edge between the blood vessel and the plaque. In Fig. 5.11b a large plaque is shown in the left part of the blood vessel. Due to the temporal smoothing inherent in the model the segmentation fails to segment the plaque. A few frames later the model correctly segments the blood vessel and the plaque.

For comparison with the 3-D images, a 2-D long axis view showing the carotid artery and the plaque is shown in Fig. 5.12. The reconstructed 3-D model is shown in Fig. 5.13a without any smoothing (no forward-backward approach and no spatial averaging are used) and in Fig. 5.13b with smoothing (forward-backward approach and spatial averaging are used).

For two patients either the method failed to segment the plaque or the blood vessel. In Fig. 5.14, such an example is shown. It should be noted that the

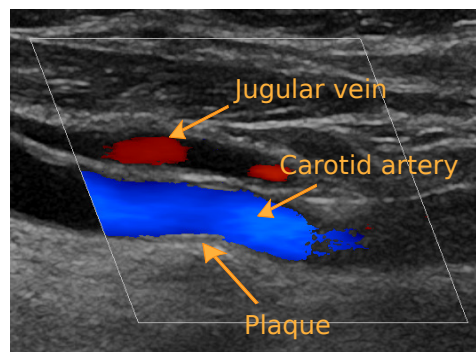
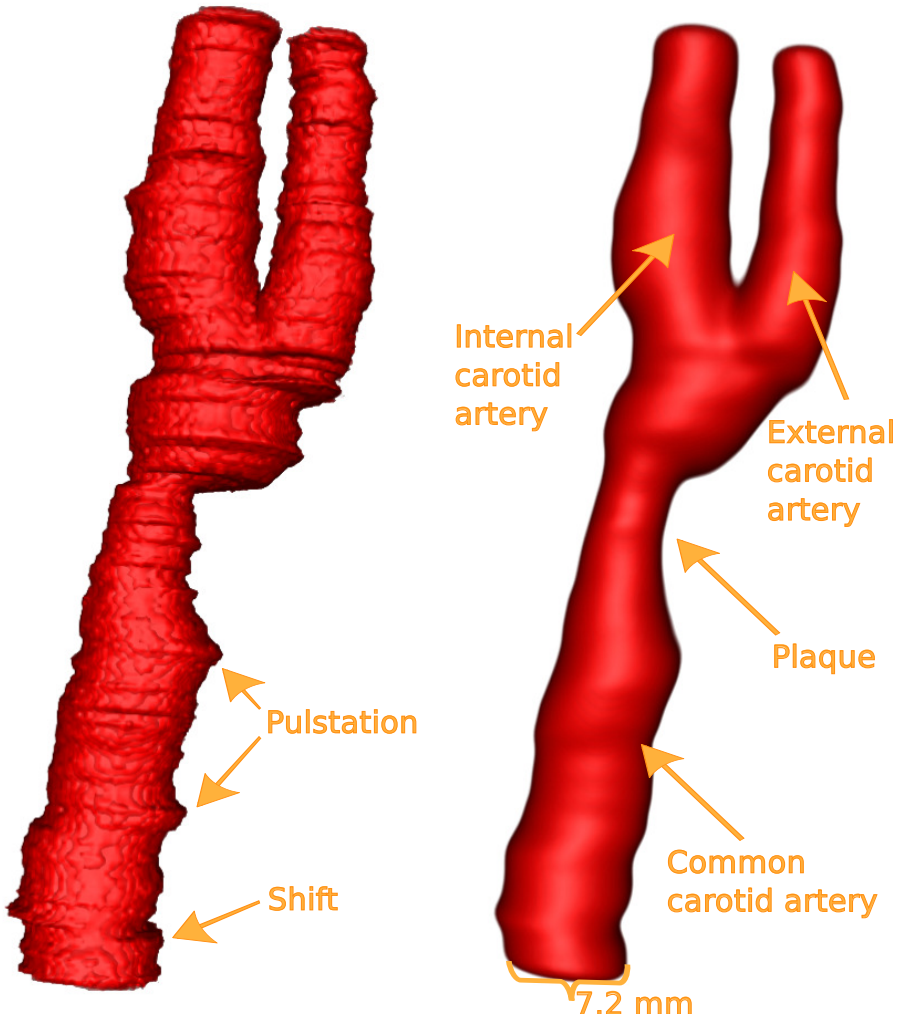


Figure 5.12: Long axis of carotid artery with plaque.



(a) Volume without any smoothing and the Kalman filter only applied forward.

(b) Volume with smoothing.

Figure 5.13: 3-D volume of carotid artery from a patient with plaque.

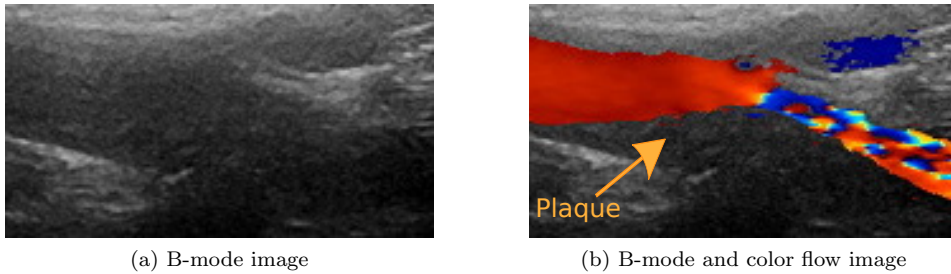


Figure 5.14: Long axis view of a plaque in the carotid artery.

hypoechoic plaque could only be detected by studying the color flow image. In Fig. 5.15, a short axis view of a case with very noisy images is shown, causing the automatic segmentation algorithm to fail.

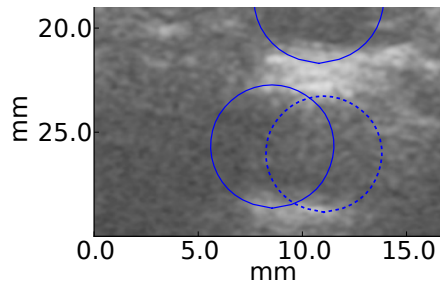


Figure 5.15: Short axis of interna and externa carotid artery. Blue solid lines are the results from the automatic segmentation and the blue dotted line is where the blood vessel actually is.

The segmentation of the 2-D frames was done using a quad core 1.87 GHz computer, and an average computation time of 72 ms per frame was achieved. Depending on the volume size the 3-D reconstruction takes about 30 seconds.

5.4 Discussion

In this work we have shown how on-the-fly segmentation of 2-D tissue images can be used in combination with a position system to generate 3-D models of the carotid artery. A 3-D model of the carotid artery could be of clinical value in providing a better visualization of the plaque degree and distribution during patient examination. Also, such a model could be the basis for estimation of plaque volume, a suggested new marker in plaque evaluation. Although indications are given for the usefulness of 3-D models of the carotid artery for visualization and flow simulations, a larger patient study is needed to properly establish the clinical

value of the method and document the robustness for a larger variation of patient cases.

To investigate the accuracy of the complete imaging and 3-D reconstruction pipeline, *in vitro* experiments using a tube with known diameter was used. The reconstructed data from the flow phantom were compared with a ground truth. The results in Tab 5.2 shows a good agreement between the automatically generated 3-D mesh and the reference. This demonstrates a high accuracy of the entire process for an idealized case.

As shown in Fig. 5.9, the errors from segmentation of the common carotid artery is in general lower than for the segmentation of the externa and interna carotid artery. This was due to noisy images and drop-outs which in some cases made it difficult to segment both the interna and externa artery. In fact, expert evaluator no. 2 only found one of the vessels after the bifurcation for two of the data sets. Considering errors above 3 mm as outliers, the inter-observer error seems to be comparable to the error of the manual segmentation compared with the automatic segmentation. In this perspective, the automatic segmentation is overall at least performing as well as manual segmentation, but the limited data set restricts us from concluding on this aspect. It should in this context be noted that while the manual segmentation was based on still images, the segmentation algorithm also incorporates information from previous frames in its final estimate.

The automatic segmentation is based on results from edge detections and block matching. So an inaccurate edge detection or block matching might lead to an inaccurate segmentation. The edge detection seems to be the most important input to the Kalman filter, and estimates the position of the vessel walls. Further, block matching can detect global movement of the vessel in the 2-D plane, caused by movement of the probe.

In the prediction step of the Kalman filter a regularization of the model is done by pulling the state vector towards the initial state. The regularization of the model must be low enough for the model to deform around plaque. Regularization of the model is also important to avoid too much influence from noise in the images. If the model was made sufficiently deformable to capture the small plaque shown in Fig. 5.11a, the model was too much influenced by noise. A compromise for the regularization was found that worked for the test cases included, but the approach may have difficulties to segment small plaques with weak edge information in general.

A correct registration of image planes is dependent on a common reference axis for both the imaging object and probe. In this work a reference frame was attached to the patient's bed, and movements inferred by swallowing or moving the head during acquisition, will give an error in the reconstructed 3-D model. Fig. 5.13a shows the 3-D model without any smoothing. In the lower part of the common carotid artery there is a small shift in the 3-D model, that we believe is caused by uncertainties in the navigation system or a movement of the carotid artery. The effect of pulsatile flow can also be seen in the figure. As mentioned the estimation of the pulsation from the automatic segmentation can be useful, but is typically not desired when visualizing the carotid artery in 3-D. In our case, by smoothing in time we are effectively also smoothing along the vessel, and the effect

of spatiotemporal pulsation is thereby reduced. The final smoothed 3-D model in Fig. 5.13b illustrates how the plaque is distributed in 3-D, and was consistent when compared to the 2-D long axis view in Fig. 5.12. As this model can be generated on-the-fly it may provide the physician with valuable clinical information during an examination. It is for instance of interest to see whether the plaque extends well into the internal carotid, complicating a potential endarterectomy. It is also of interest to get an impression of the plaque volume for risk assessment [22].

Reverberations from tissue structures add noise and lower contrast resolution in the ultrasound images, this can for instance be seen in Fig. 5.8. With too much noise in the images the algorithm will fail to segment the plaque, and in the worst case the segmentation of the blood vessel will fail altogether. In Fig. 5.14a the plaque is close to invisible on the B-mode image, and with high probability both automatic and manual segmentation will fail. In general, a soft plaque is often hypoechoic, and is especially challenging to detect in the presence of substantial acoustic noise. A color-Doppler image is then currently needed to be able to detect the regions of stenosis, as shown in Fig. 5.14b. The information in the color flow image can be added to further improve the segmentation. The edge detection and block matching can be done both on the B-mode and the corresponding color flow image, and the displacement vector from both images can then be included in the update step given in Eqn. (5.2). But also the color flow image has limitation due to artifacts from drop-outs, aliasing and angle dependencies. In future work the color flow image could also be used to eliminate the need for defining manual seed points.

From an estimated diameter variation the relative pressure can be estimated, which when for instance calibrated towards peripheral mean pressure measurement can be used as input in a computational fluid dynamic simulations (CFD) [23]. Further work should study how well suited the 3-D mesh from the algorithm is for patient specific flow simulations of the carotid artery, for improved understanding of how plaques develop in the carotid artery.

The carotid circumferential strain can also be calculated from the available data, and is associated with risk of incident ischemic stroke [24]. Fig. 5.7 shows how the estimated diameter repeats consistently for each cycle. The shape of the diameter-curve corresponds well with results found in literature, corresponding to a distensibility of about 15% for a healthy volunteer (26 years old) [25].

In some cases the automatic segmentation may fail due to noisy images, and a semi-automatic approach is needed to correct the model. To avoid massive user input, sparse corrections could also be used as spatial attractors when running the segmentation model once more to increase accuracy and robustness. This approach however, remains to be tried. A semi-automatic approach is then required for a successful segmentation. In Fig. 5.15 an example of a noisy lumen with poor delineation of the edges is shown. This may be the case for parts of the carotid artery, typically in the bifurcation and more distal parts.

5.5 Conclusion

On-the-fly 3-D reconstruction of the carotid artery based on navigated 2-D B-mode imaging was feasible using a Kalman filter segmentation approach. A patient study ($N = 5$) revealed that the automatic segmentation may be as good as a manual segmentation when considering interobserver variability, resulting in an error of 0.84 mm measured by the modified Hausdorff distance. The bedside 3-D reconstruction of the carotid artery can be useful by providing additional information of plaque volume and extents for risk assessment, and may also provide a basis for rapid patient specific computational fluid simulations and analysis in the future.

REFERENCES

- [1] G. A. Donnan, M. Fisher, M. Macleod, S. M. Davis, S. Royal, and U. K. M. Macleod, "Stroke," *Lancet*, vol. 371, no. 9624, pp. 1612–1623, 2008.
- [2] J. Bamford, P. Sandercock, M. Dennis, C. Warlow, and J. Burn, "Classification and natural history of clinically identifiable subtypes of cerebral infarction," *The Lancet*, pp. 1521–1526, 1991. [Online]. Available: <http://www.sciencedirect.com/science/article/pii/0140673691932060>
- [3] B. F. I, S. Zhang, O. S. I, J. Suri, J. S. Lewin, D. L. Wilson, and A. R. Algorithm, "Three-Dimensional Automatic Volume Registration of Carotid MR Images," *Proceedings of the 25th Annual International Conference (IEEE Engineering in Medicine and Biology Society)*, vol. 1, pp. 646–648, 2003.
- [4] P. Slomka, J. Mandel, D. Downey, and A. Fenster, "Evaluation of voxel-based registration of 3-D power Doppler ultrasound and 3-D magnetic resonance angiographic images of carotid arteries," *Ultrasound in medicine & ...*, vol. 27, no. 7, pp. 945–955, 2001. [Online]. Available: <http://www.sciencedirect.com/science/article/pii/S0301562901003878>
- [5] A. Landry, C. Ainsworth, C. Blake, and J. D. Spence, "Manual planimetric measurement of carotid plaque volume using three-dimensional ultrasound imaging," *Medical physics*, vol. 34, pp. 1496–1505, 2007.
- [6] C. D. Ainsworth, C. C. Blake, A. Tamayo, V. Beletsky, A. Fenster, and J. D. Spence, "3D ultrasound measurement of change in carotid plaque volume: a tool for rapid evaluation of new therapies." *Stroke; a journal of cerebral circulation*, vol. 36, no. 9, pp. 1904–9, Sep. 2005. [Online]. Available: <http://www.ncbi.nlm.nih.gov/pubmed/16081857>
- [7] B. Chiu, M. Egger, J. D. Spence, G. Parraga, and A. Fenster, "Quantification of carotid vessel wall and plaque thickness change using 3D ultrasound images," *Medical Physics*, vol. 35, no. 8, p. 3691, 2008. [Online]. Available: <http://link.aip.org/link/MPHYA6/v35/i8/p3691/s1&Agg=doi>
- [8] F. Mao, J. Gill, D. Downey, and A. Fenster, "Segmentation of carotid artery in ultrasound images: Method development and evaluation technique," *Medical physics*, pp. 11–16, 2000. [Online]. Available: <http://link.aip.org/link/mphysa6/v27/i8/p1961/s1>

-
- [9] A. Blake, R. Curwen, and A. Zisserman, "A framework for spatiotemporal control in the tracking of visual contours," *International Journal of Computer Vision*, vol. 11, no. 2, pp. 127–145, Oct. 1993. [Online]. Available: <http://link.springer.com/10.1007/BF01469225>
- [10] G. Jacob, J. a. Noble, M. Mulet-Parada, and a. Blake, "Evaluating a robust contour tracker on echocardiographic sequences." *Medical image analysis*, vol. 3, no. 1, pp. 63–75, Mar. 1999. [Online]. Available: <http://www.ncbi.nlm.nih.gov/pubmed/10709697>
- [11] F. Orderud and S. I. Rabben, "Real-time 3D segmentation of the left ventricle using deformable subdivision surfaces," *2008 IEEE Conference on Computer Vision and Pattern Recognition*, pp. 1–8, Jun. 2008. [Online]. Available: <http://ieeexplore.ieee.org/lpdocs/epic03/wrapper.htm?arnumber=4587442>
- [12] S. R. Snare, O. C. Mjølstad, F. Orderud, H. v. Dalen, and H. Torp, "Automated septum thickness measurement—a Kalman filter approach." *Computer methods and programs in biomedicine*, vol. 108, no. 2, pp. 477–86, Nov. 2012. [Online]. Available: <http://www.ncbi.nlm.nih.gov/pubmed/21477880>
- [13] F. Orderud, "A framework for real-time left ventricular tracking in 3D+T echocardiography, using nonlinear deformable contours and kalman filter based tracking," *Computers in Cardiology, 2006*, pp. 125–128, 2006. [Online]. Available: http://ieeexplore.ieee.org/xpls/abs_all.jsp?arnumber=4511804
- [14] C. Askeland, F. Lindseth, O. V. Solberg, J. Beate, L. Bakeng, and G. A. Tangen, "CustusX : A Research Application for Image-Guided Therapy," *Insight Journal*, pp. 1–8, 2011.
- [15] F. Lindseth, T. Langø, J. Bang, and T. N. Hernes, "Accuracy evaluation of a 3D ultrasound-based neuronavigation system." *Computer aided surgery : official journal of the International Society for Computer Aided Surgery*, vol. 7, no. 4, pp. 197–222, Jan. 2002. [Online]. Available: <http://www.ncbi.nlm.nih.gov/pubmed/12454892>
- [16] B. Lucas and T. Kanade, "An iterative image registration technique with an application to stereo vision." *IJCAI*, vol. 130, pp. 121–130, 1981. [Online]. Available: http://flohauptic.googlecode.com/svn-history/r18/trunk/optic_flow/docs/articles/LK/Barker_unifying/lucas_bruce_d.1981.2.pdf
- [17] F. Orderud, G. Kiss, S. Langeland, E. W. Remme, H. G. Torp, and S. I. Rabben, "Combining edge detection with speckle-tracking for cardiac strain assessment in 3D echocardiography," *2008 IEEE Ultrasonics Symposium*, pp. 1959–1962, Nov. 2008. [Online]. Available: <http://ieeexplore.ieee.org/lpdocs/epic03/wrapper.htm?arnumber=4803187>
- [18] O. V. Solberg, F. Lindseth, H. Torp, R. E. Blake, and T. a. Nagelhus Hernes, "Freehand 3D ultrasound reconstruction algorithms—a review." *Ultrasound*

REFERENCES

- in medicine & biology*, vol. 33, no. 7, pp. 991–1009, Jul. 2007. [Online]. Available: <http://www.ncbi.nlm.nih.gov/pubmed/17512655>
- [19] V. Chalana and K. Yongmin, “A Methodology for Evaluation of Boundary Detection Algorithms on Medical Images,” *IEEE transactions on medical imaging*, vol. 16, no. 5, pp. 642–652, May 1997.
- [20] D. P. Huttenlocher, G. A. Klanderman, and W. J. Rucklidge, “Comparing images using the Hausdorff distance,” *Pattern Analysis and Machine Intelligence, IEEE Transactions on*, vol. 15, no. 9, pp. 850–863, 1993. [Online]. Available: http://ieeexplore.ieee.org/xpls/abs_all.jsp?arnumber=232073
- [21] M. Dubuisson and A. Jain, “A modified Hausdorff distance for object matching,” *Pattern Recognition, 1994. Vol. 1- ...*, no. 1, pp. 566–568, 1994. [Online]. Available: http://ieeexplore.ieee.org/xpls/abs_all.jsp?arnumber=576361
- [22] S. Rozie, T. T. de Weert, C. de Monyé, P. J. Homburg, H. L. J. Tanghe, D. W. J. Dippel, and a. van der Lugt, “Atherosclerotic plaque volume and composition in symptomatic carotid arteries assessed with multidetector CT angiography; relationship with severity of stenosis and cardiovascular risk factors.” *European radiology*, vol. 19, no. 9, pp. 2294–301, Sep. 2009. [Online]. Available: <http://www.pubmedcentral.nih.gov/articlerender.fcgi?artid=2719076&tool=pmcentrez&rendertype=abstract>
- [23] I. E. Vignon-Clementel, C. A. Figueroa, K. E. Jansen, and C. A. Taylor, “Outflow boundary conditions for three-dimensional finite element modeling of blood flow and pressure in arteries,” *Computer Methods in Applied Mechanics and Engineering*, vol. 195, no. 2932, pp. 3776–3796, 2006. [Online]. Available: <http://www.sciencedirect.com/science/article/pii/S0045782505002586>
- [24] E. Y. Yang, L. Chambless, a. R. Sharrett, S. S. Virani, X. Liu, Z. Tang, E. Boerwinkle, C. M. Ballantyne, and V. Nambi, “Carotid arterial wall characteristics are associated with incident ischemic stroke but not coronary heart disease in the Atherosclerosis Risk in Communities (ARIC) study.” *Stroke; a journal of cerebral circulation*, vol. 43, no. 1, pp. 103–8, Jan. 2012. [Online]. Available: <http://www.pubmedcentral.nih.gov/articlerender.fcgi?artid=3246524&tool=pmcentrez&rendertype=abstract>
- [25] F. Hansen, P. Mangell, B. Sonesson, and T. Länne, “Diameter and compliance in the human common carotid artery variations with age and sex,” *Ultrasound in medicine & ...*, vol. 21, no. 1, pp. 1–9, 1995. [Online]. Available: <http://www.sciencedirect.com/science/article/pii/0301562994000905>

